

Article

Experimental and Kinetic Study of the Catalytic Behavior of Sulfate-Treated Nanostructured Bifunctional Zirconium Oxide Catalysts in *n*-Heptane Hydroisomerization Reactions

Mohammed Khalil¹, Bashir Y. Al-Zaidi¹ , Zaidoon M. Shakor¹ , Sattar J. Hussein² and Ali Al-Shathir^{1,*} 

¹ Department of Chemical Engineering, University of Technology - Iraq, Alsinaa Street 52, Baghdad 10066, Iraq; che.20.08@grad.uotechnology.edu.iq (M.K.); bashir.y.sherhan@uotechnology.edu.iq (B.Y.A.-Z.); zaidoon.m.shakor@uotechnology.edu.iq (Z.M.S.)

² Research and Development Center, Ministry of Oil - Iraq, Baghdad 00964, Iraq; sattar.refining@prdc.oil.gov.iq

* Correspondence: ali.r.mohammedjawad@uotechnology.edu.iq

Abstract: In this study, a mono-functional ZrO₂ nanomaterial was treated with sulfur and loaded with two different percentages of platinum metals (i.e., 0.5 and 1 wt%) to generate an acidic bi-functional Pt/SZrO₂ nanocatalyst for the purpose of increasing the catalytic activity and selectivity together. This work aims to determine the least amount of the costly platinum metal that can be added to the catalyst to achieve the appropriate balance between the acidic and metallic sites. Both rapid deactivation of the super-acid nanocatalyst and fast cleavage of the zero-octane *n*-heptane chain can consequently be prevented throughout the reaction. This can be achieved by accelerating the hydroisomerization reactions at a pressure of 5 bar to reach the highest selectivity towards producing the desired multi-branched compound in fuel. Several characterization techniques, including XRD, SEM, EDX, BET, and FTIR, have been used to evaluate the physical properties of the catalysts. The best reaction product was obtained at 230 °C compared to the other tested temperatures. The conversion, selectivity, and yield of reaction products over the surfaces of the prepared catalysts followed this order: 0.5 wt% Pt/SZrO₂ > 1 wt% Pt/SZrO₂ > 0.5 wt% Pt/ZrO₂ > 1 wt% Pt/ZrO₂ > SZrO₂ > ZrO₂. The highest conversion, selectivity, and yield values were obtained on the surface of the 0.5 wt% Pt/SZrO₂ catalyst, which are 69.64, 81.4 and 56.68 wt%, respectively, while the lowest values were obtained on the surface of the parent ZrO₂ catalyst, which are 43.9, 61.1 and 26.82, respectively. The kinetic model and apparent activation energies were also implemented for each of the hydroisomerization, hydrogenation/dehydrogenation, and hydrocracking reactions, which track the following order: hydroisomerization < hydrogenation/dehydrogenation < hydrocracking. The lowest apparent activation energy value of 123.39 kJ/mol was found on the surface of the most active and selective 0.5% Pt/SZrO₂ nanocatalyst.

Keywords: bi-functional Pt/SZrO₂ nanocatalyst; sulfate treatment; Pt-metal loading by impregnation; *n*-heptane hydroisomerization reactions; kinetic model



Citation: Khalil, M.; Al-Zaidi, B.Y.; Shakor, Z.M.; Hussein, S.J.; Al-Shathir, A. Experimental and Kinetic Study of the Catalytic Behavior of Sulfate-Treated Nanostructured Bifunctional Zirconium Oxide Catalysts in *n*-Heptane Hydroisomerization Reactions. *ChemEngineering* **2023**, *7*, 115. <https://doi.org/10.3390/chemengineering7060115>

Academic Editor: Alirio E. Rodrigues

Received: 16 October 2023

Revised: 19 November 2023

Accepted: 27 November 2023

Published: 1 December 2023



Copyright: © 2023 by the authors. Licensee MDPI, Basel, Switzerland. This article is an open access article distributed under the terms and conditions of the Creative Commons Attribution (CC BY) license (<https://creativecommons.org/licenses/by/4.0/>).

1. Introduction

The technical and environmental quality of fuel must be taken into account during the development of clean gasoline for today's engines. In fact, high octane fuel, in the range of 87 to 95 with a low environmental impact, is necessary to obtain optimal gasoline. Compared to aromatics or olefins, the family of alkanes as a whole has much less photochemical reactivity, but only highly branched alkanes have satisfactory octane numbers for use as fuel. Due to the fact that the alkanes in the gasoline fraction of crude oil are mostly linear or monobranched, they must be isomerized and reformatted to create highly branched isomers. In order to increase the octane number of gasoline in the petroleum refining process, it is important to isomerize butane, pentane, and hexane; however, this technology has not been applied to *n*C₇ and heavier alkanes because the formation of cracking products

risers very quickly as conversion increases. The need to produce clean fuels with high octane ratings has prompted researchers to search for new solid catalysts with improved selectivity for nC_7^+ isomers [1]. Depending on the processing conditions, zirconium oxide, or zirconia, can be modified into an acidic or super acidic catalyst by adding anions such as sulfate ions. This catalyst has been found to be highly suitable for catalyzing processes of industrial importance, such as hydrocarbon isomerization, cracking/hydrocracking reactions, conversion of methanol to hydrocarbons, alkylation, esterification, cyclization, hydrogenation-dehydrogenation reactions, oxidation, oligomerization, etc. In cooperation with noble metals such as platinum loaded onto the catalysts, the surface characteristics of these catalysts can be further modified by increasing their catalytic efficiency [2]. Sulfates increase the structural stability of zirconia, lower reaction temperatures, and enhance thermal stability when added [3]. The activity of solid acid catalysts is influenced by the properties of the active sites (i.e., Brønsted and Lewis acids), as well as other factors including the nature of the starting materials and the procedures used for thermal treatment [4]. In fact, the acidic properties of the oxide surface can be significantly changed by simple modification of the preparation steps [5,6]. The calcination temperature and sulfur agent concentration affect the catalytic performance of sulfated zirconia [7]. According to Busto et al. [8], the acidity distribution is affected by the calcination temperature variables, and the maximum concentration of acid sites and activity levels can be produced at the optimum calcination temperature. Under these ideal conditions, it was found that sulfated zirconia enhanced the amount of acidity and increased the catalytic activity of the catalysts [9]. However, these super-acid solid catalysts are often quickly deactivated. It is known that some ultra-acid solid catalysts catalyze the skeletal isomerization of hydrocarbons at low temperatures for a certain period throughout the reaction. Sulfated zirconia (SZ), for example, is a very strong acid solid that can catalyze *n*-hexane isomerization at ambient temperatures even in the absence of metal sites, although it is deactivated very quickly. There have been a number of hypotheses put forward to explain the rapid deactivation of the catalyst, including loss of sulfur, sulfur oxidation state changes, crystal structural transformations, and deposition of hydrocarbon fragments. In fact, the sulfur content is likely to have an effect on the crystal structure and activity of the catalyst [10,11]. In addition, sulfate groups slow the crystallization process in amorphous zirconia [3] by means of relieving some of the surface energy and stabilizing its phase. Platinum has also been shown to enhance the stability of SZ catalysts [12–15], and hydrogen must be present throughout the reaction to maintain the catalytic activity of the catalysts. According to the authors [15,16], strong protonic acidity is produced by the dissociation, diffusion, and conversion of hydrogen species into hydrides, which accelerates the adsorption of carbenium intermediates, and this process includes a chain initiation step with loss of hydrogen from alkanes, a carbenium ion isomerization step, and a carbenium ion diffusion step that involves the transfer of hydrogen from a neutral molecule to a carbocation (i.e., carbon cations), which leads to the removal of the isomeric carbocation from the surface and the formation of a new carbocation. The long residence times of hydrocarbon chains on the catalyst surface and the high probability of cleavage via β -scission reactions result from carbocation desorption being slow and limited by the rate of hydrogen transfer, especially for *n*-heptane and higher alkanes where oligomerization is not necessary for the β -scission reaction to proceed. In the steady state, the surface isomerization process is approximately equilibrated and nearly saturated with carbocations [12]. Methods of preparing sulfurized zirconia by wet impregnation techniques using zirconium oxide, zirconyl nitrate hydrate, zirconium oxychloride octahydrate, and zirconium hydroxide as a precursor have been previously presented in the published literature [15,17–22]. The stabilizing properties of sulfate ions on the surface of zirconia, which promote the formation of the tetragonal crystalline phase at calcination temperatures exceeding 540 °C, are the reason for the increased activity of sulfated zirconia. However, as mentioned previously, the rapid deactivation of these catalysts has prevented their application in industrial processes, and more recent research has focused on reducing this effect. Transition metals including Ni, Pt, Pd, Rh, Ru, Co, W, and Mo were also added

to the sulfated zirconia to solve the deactivation problem. It has been proven through practical experiments that Pt is present on the catalyst surface in the form of metallic Pt that can maintain its activity even at calcination temperatures of 600 °C and above, and these metallic Pt centers are active sites for *n*-butane and *n*-hexane isomers. On the other hand, Pt contributes to the increased acidity of the Pt/sulfate zirconia catalysts. The hydrogen molecule splits into hydrogen atoms at Pt sites before spilling into sulfated zirconia, where H⁻ formation on the Lewis acid site converts the H-atom into H⁺. It was then proposed that H⁺ serves as the acidic site for the *n*-alkane isomerization [22]. In addition, it has been documented that adding a small percentage of metal can enhance the Lewis acidity of catalysts [23,24].

The importance of Brønsted acid sites has been carefully studied, and acid strength is probably the most important element in isomerization activity. In order to understand the nature of the active sites, the behavior of the surface structure of Pt/SZ on different structures of catalysts was investigated. Oloye studied the conversion of *n*-Heptane via a Pt/sulfated zirconia catalyst using a fixed-bed reactor under atmospheric pressure at reaction temperatures ranging between 453 and 723 K. It has been found that the formation of cracked products occurs only at higher conversion levels through successive reaction routes [25]. Alemán-Vázquez found that the sulfated zirconia catalyst has super-acidic properties by evaluating Pt/sulfated zirconia in an experimental system for *n*-heptane isomerization, and noted that it has good activity for the isomerization reaction of alkanes, but is subject to rapid deactivation [10]. Busto tested the isomerization-cracking of long-chain *n*-paraffins using commercial Pt/SO₄₂-ZrO₂ catalysts and found that increasing temperature values increased the conversion but also increased the cracking. Therefore, the optimum values were obtained at a moderate temperature of 225 °C for high feed reactivity [8]. Song used three Pt-promoted sulfated zirconia catalysts. It was proposed that the presence of excessive sulfur species on the sample was suitable to maintain active sulfur at the catalyst surface [17]. Vijay used a Pt-promoted sulfated zirconia (SZ) catalyst with a highly active catalyst for *n*-pentane isomerization under atmospheric conditions. Note that upon repeated regeneration processes, the conversion increases with *iso*-pentane selectivity, as the duplicated oxidation/reduction cycles lead to restructuring of the acid and metal sites, facilitating hydrogen migration and helping to reduce or stop catalyst deactivation [15].

The aim of this work is to investigate the effect of both sulfate pretreatments to activate acid sites as well as platinum metal loading to activate metal sites on the catalytic performance of cheap zirconium oxide (ZrO₂) nanocatalysts during *n*-heptane hydroisomerization reactions. This study conducted a comprehensive comparison between the catalytic activities and catalytic selectivities of the prepared nano-catalysts before and after metal loading and/or sulfate treating. The goal was to reach the best degree of balance between the acidic sites and the metallic sites within the structural framework of nanocatalysts for the purpose of producing the highest percentage of isomers and the highest yield through avoiding the deactivation problem that most super-acid solid catalysts used in this type of reaction suffer from. In order to fill the gap in the published literature in this field, the effect of reaction temperature was also studied, and a mathematical model was developed to calculate the values of apparent activation energies for each of the hydroisomerization, hydrogenation/dehydrogenation, and hydrocracking reactions with the aim of comparing their values with the experimental results of the produced spectra of hydrocarbons.

2. The Experimental Work

2.1. Materials

Table 1 provides an overview of the different types of chemicals employed in the experimental aspect of this study.

Table 1. Chemical reagents and their commercial sources.

No.	Material	Composition	Company	Origin	Purity
1	Zirconium Oxide Nanoparticles	ZrO ₂	US Research Nanomaterials, Inc	USA	99.+%
2	Hydro-HexachloroPlatinic Acid	(H ₂ PtCl ₆)·6H ₂ O	Direvo Industrial Biotechnology	Germany	99%
3	<i>n</i> -Heptane	CH ₃ (CH ₂) ₅ CH ₃	J.T. Baker	USA	99%
4	Sulfuric Acid	H ₂ SO ₄	J.T. Baker	USA	98%
5	Hydrogen Gas	H ₂	Petroleum Research and Development Center	Iraq	99.9%
6	Deionized Water	H ₂ O	University of Technology—Baghdad	Iraq	99.99%

2.2. The Characterization Techniques

X-ray diffraction (XRD) analysis was conducted using a Panalytical X'Pert Pro XRD instrument of the Cu K α anode type with a wavelength of 1.54 Å which was from the UK. The detector employed is the X'Celerator, an ultra-fast X-ray detector, which operates on Real Time Multiple Strip (RTMS) technology. Scanning electron microscopy (SEM) was used to obtain the structural morphologies of the catalysts. This was achieved utilizing a TESCAN type, MIRA3 XMU, Brno, Czech Republic. The BRUKER Inspect S50 instrument provides the use of energy dispersive X-ray spectroscopy (EDAX) to determine the elemental compositions present within the surface of a given material. The surface areas of the as-synthesized catalysts were measured using the Brunauer-Emmett-Teller (BET) technique, utilizing a HORIBA SA-9600 instrument for gas adsorption-desorption isothermal analysis. The use of Fourier transform infrared spectroscopy (FTIR) allows for the characterization of chemical bonds and functional groups within materials. In this study, a SHIMADZU IR PRESTIGE-21 FTIR microscope, AIM-8800, Kyoto, Japan, was applied for this purpose.

2.3. Bifunctional Nanocatalyst Preparation

The metal solution used for platinum loading is prepared by dissolving 1 g of the metal salt of hexahydrate of chloroplatinic acid, H₂PtCl₆·6H₂O, in 100 mL of deionized water. This dissolution process is carried out using a magnetic mixer at a temperature of 65 °C for one hour. The resulting solution is then used for the purpose of depositing platinum metal on the nano-particles of a catalyst by the impregnation method [26]. It must be added carefully and gradually to the zirconia oxide while continuously stirring for 2 h at a temperature of 75 °C. The required amounts of deionized water drops are also added to obtain a homogeneous solution. The obtained sample was then subjected to drying overnight at 110 °C, according to metal loading techniques documented in the literature [27]. Two different weight percentages of platinum metal, namely 0.5 and 1 wt%, were loaded onto the porous surface of zirconium oxide nanoparticles. To be precise, the specific percentage values of the loaded platinum metal measured from EDX analysis within the ZrO₂ and SZrO₂ samples were 0.52, 1.14, 0.48, and 0.97 wt%, which closely mimics the assumed theoretical percentages of 0.5 and 1 wt% in both samples, respectively. In fact, the sulfur precursor solution was produced through a sulfurization process which involves treating ZrO₂ nanoparticles with a 0.1 M aqueous solution of sulfuric acid [H₂SO₄] to prepare sulfated zirconia denoted as [SZrO₂]. It should be noted that sulfate treatment must be carried out before loading platinum onto the surface of catalysts because it requires a high calcination temperature. This treatment took approximately 12 h with continuous mixing at room temperature. The samples were then dried in an oven at 110 °C for a full day. For the purpose of performing the calcination process, the sample is then heated to the calcination temperature of 700 °C. The purpose of this pretreatment is to enhance the acidity of the nanocatalyst, which promotes the catalytic activity of hydrocarbon isomerization reactions on its surface [5]. Next, the [SZrO₂] particles were isolated and subjected to a 24-h drying process to be ready for the deposition of platinum metal on their surface using the previously described methodology. The method that was used to prepare sulfated and/or unsulfated bifunctional zirconia nanocatalysts that were utilized in *n*-heptane

hydroisomerization reactions can be summarized by the schematic diagram shown in Figure 1.

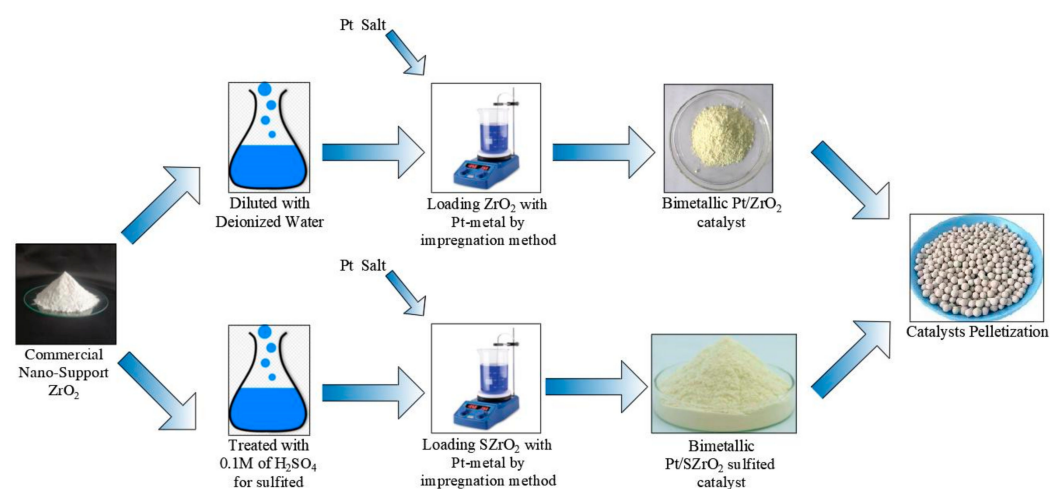


Figure 1. Summary of the steps followed in the catalyst preparation procedures.

Catalyst Pelletizing

The prepared Pt/ZrO₂ and Pt/SZrO₂ catalysts were pelletized by pressing the solid powder of the dry sample, resulting in the formation of small circular discs. This process was carried out using a hydraulic press, where the powder was compressed at a pressure of about 15 tones/m² [28]. The circular disc formed then underwent grinding and sieving processes to reach the desired particle size using a sieve mesh with dimensions ranging from 125 to 300 μm and then the catalysts were packed into the reactor. It should be noted that the use of catalyst pellets with geometric shapes, including spherical ones, helps in avoiding a sudden drop in pressure inside the reactor bed while conducting hydroisomerization experiments.

2.4. Experimental Catalytic Reactions

Catalytic hydroisomerization of *n*-heptane has been performed via several nano-structured catalysts supported by different proportions of Pt-metal, as exposed in Table 2.

Table 2. Abbreviations for the types of catalysts used in reactions.

No.	Catalyst Code	Catalysts Type
1	Cat-1	Unsulphated Zirconium Oxide; [ZrO ₂]
2	Cat-2	[ZrO ₂] loaded with 0.5% Pt; [0.5% Pt/ZrO ₂]
3	Cat-3	[ZrO ₂] loaded with 1% Pt, [1% Pt/ZrO ₂]
4	Cat-4	Sulphated Zirconium Oxide; [SZrO ₂]
5	Cat-5	[SZrO ₂] loaded with 0.5% Pt; [0.5% Pt/SZrO ₂]
6	Cat-6	[SZrO ₂] loaded with 1% Pt, [1% Pt/SZrO ₂]

A fixed-bed reactor made of stainless steel with an inner diameter of 10 mm and a length of 30 cm was used. Catalyst particles weighing approximately 6 g with diameters ranging from 125 to 300 μm were packed into the reactor core within the stable temperature zone. The catalyst was placed between two layers of 3 mm diameter ceramic spherical beads. These beads are typically used to stabilize the catalyst and occupy the empty space inside the reactor in order to regulate the thermal distribution of the reactant molecules prior to thermal decomposition—generally after the reactants have been transferred to the surface of catalyst particles. In fact, before the reaction starts, the metals on the catalyst surface are reduced in situ, and the reduction process takes place at a pressure of 5 bar under a hydrogen flow rate of 5 L/h at a temperature of 450 °C for 3 h [29,30]. Subsequently, the reactor undergoes a continuous cooling process until its temperature reaches

the hydroisomerization reaction temperature of 230 °C. A dosing pump is a kind of positive displacement pump that is specially designed to inject a certain amount of chemicals with high precision into a gas or liquid stream. At the beginning of the experiment, the dosing pump is activated to pump the *n*-heptane feed, which has a boiling point of about 98.4 °C in its liquid phase at a flow rate of 20 mL/h. After that, the feed stream combines with the hydrogen gas stream and finally reaches the catalyst bed to initiate the hydroisomerization reaction. The reaction products are condensed utilizing a purpose-built condenser, operating at low enough temperatures to condense all the resulting hydrocarbons. Condensed hydrocarbons are collected continuously over a period of one hour and are subjected to analysis using a chromatographic analyzer equipped with a flame ionization detector (FID) to determine the types of hydrocarbon components generated by the reaction. A mathematical formula [25] was applied to determine conversion (*X*), selectivity (*S*), and yield (*Y*), as follows:

$$\%X = \frac{X_i - X_f}{X_i} \times 100 \quad (1)$$

$$\%S = \frac{X_n}{X_i - X_f} \times 100 \quad (2)$$

$$\%Y = \%X \times \%S = \frac{x_n}{x_i} \times 100 \quad (3)$$

In this context, X_i represents the initial quantity of *n*-heptane (μmol), X_f represents the quantity of unreacted *n*-heptane, and X_n represents the quantity of the individual product.

A series of tests were performed to evaluate the catalytic performance of the synthesized Pt/ZrO₂ and Pt/SZrO₂ catalysts using the hydroisomerization system shown schematically in the block diagram in Figure 2. The selection of optimal reaction conditions in this study was determined by a series of pilot experiments conducted under different conditions utilizing the ranges of reaction conditions documented in the published literature [1,10,25,31]. In addition, a material balance was carried out to calculate the amounts of the non-condensable gases produced from the reaction such as C₁ and C₂. This was achieved by comparing the weight of liquid *n*-heptane introduced as feed with the total weight of the condensed liquid products. The analysis revealed that the presence of light gases is nearly negligible, primarily due to effective condensation procedures.

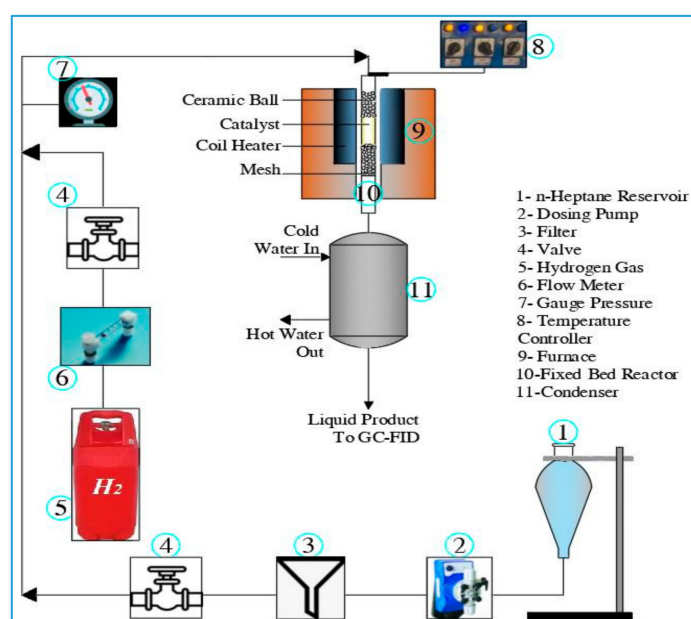


Figure 2. Schematic diagram of the experimental system for the hydroisomerization process.

3. Results Discussion

3.1. Catalysts Characterization

3.1.1. X-ray Diffraction Analysis

Structural frameworks of the as-prepared Pt/ZrO₂ and/or Pt/SZrO₂ nanocatalysts loaded with different platinum metal percentages were analyzed by applying X-ray diffraction analysis. Figure 3 displays the XRD patterns, and it is observed that according to the positions of 2θ coordinates, they match the XRD patterns reported in previous studies by Utami [5], Song [17], Ait Rass [32], and Tang [33]. In addition, the XRD-patterns of catalysts after metal loading and/or sulfate treatment show similarity to those of catalysts without any metal loading and/or sulfate treatment (i.e., traditional parent ZrO₂ and/or SZrO₂ samples).

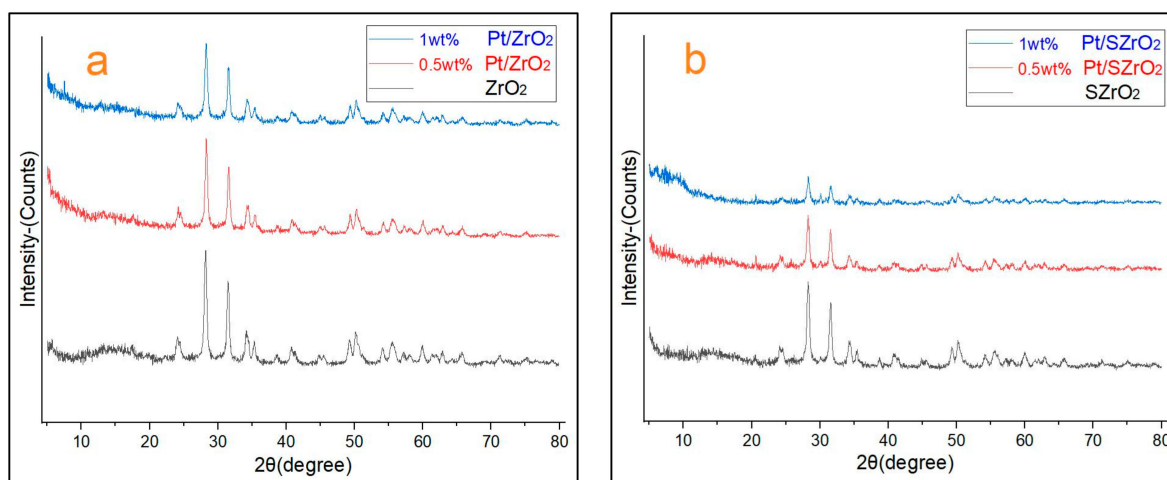


Figure 3. (a) XRD patterns of ZrO₂ and Pt/ZrO₂ samples, (b) XRD patterns of SZrO₂ and Pt/SZrO₂ samples.

The percentage crystallinity of the samples was calculated from the sum of the intensities of the main peaks provided by the XRD machine according to Equation (4) [29]. The calculations are achieved by dividing the sum of the main peak intensities of the either as-prepared Pt/ZrO₂ or Pt/SZrO₂ sample by the sum of the main peak intensities of the reference sample (i.e., parent ZrO₂ or SZrO₂ catalyst). Tables in the Supplementary File show the degree of crystallinity of the samples. It was found that the degree of crystallinity (DOC %) of ZrO₂ (as a reference sample), 0.5 wt% Pt/ZrO₂, and 1 wt% Pt/ZrO₂ are 100, 89.5, and 79.9%, respectively, while the DOC% of SZrO₂ (as a reference sample), 0.5 wt% Pt/SZrO₂, and 1 wt% Pt/SZrO₂ are 100, 94.75, and 93.13%, respectively. It must be taken into account that the degree of crystallinity decreases significantly after sulfate treatment, and the percentages that were calculated for the degrees of crystallinity of the treated catalysts were based on comparisons with the parent SZrO₂ sample. The satisfactory values of the degree of crystallinity found for the catalyst samples after metal loading and/or sulfite treatment compared to the degree of crystallinity of the parent samples confirm that the framework structures of the prepared samples maintain acceptable purity and also prove that there is no deep collapse in their framework structures.

$$(\text{DOC})\% = \frac{\text{Sum of main peak intensities of the modified sample}}{\text{Sum of main peak intensities of the reference sample}} \times 100 \quad (4)$$

No diffraction peaks resulting from the dispersion of Pt metals on the surface of Pt/ZrO₂ and or Pt/SZrO₂ catalysts were observed when the Pt loading was less than or equal to 1 wt%. This is owing to the small size of the Pt nanoparticles and their low loading, which means that the Pt diffraction peaks are too broad and have too low intensity to be detected. These results are consistent with results reported by other authors [17,33]. In

addition, a change in the relative intensity of multiple diffraction peaks was observed after metal loading and/or sulfite treatment, which is due to the fact that these loaded transition metals can act as impurities so they could cause X-ray deflection causing a decrease in peak intensity [34,35]. On the other hand, the sulfur treatment techniques for the structure of porous solids can lead to a rearrangement of atoms within the crystal lattice, causing a transition from a face-centered cubic (FCC) to a body-centered cubic (BCC) structure or vice versa [36]. Therefore, decreased solid crystallinity or partial destruction and increased amorphous materials can be expected. Moreover, the flat baseline that appeared in the XRD patterns of Pt/ZrO₂ and/or Pt/SZrO₂ seems to be higher due to the amorphous component appearing as a clearly visible halo in the range of 10–20 of 2θ coordinates as well as the by-product peaks (e.g., peaks at 21 and 32 of 2θ coordinates) in the XRD of the samples. This observation is attributed to the reduction in metals on the catalyst surface as well as the calcination of zirconium oxide structure at high temperatures during the sulfite pretreatments wherein the sulfate ions on the surface of zirconia promote the formation of the tetragonal crystalline phase.

3.1.2. Scanning Electron Microscope Analysis

A scanning electron microscope (SEM) technique was utilized to study the surface morphologies of the Pt/ZrO₂ and Pt/SZrO₂ catalysts at different magnifications (i.e., 200 nm and 1 μm). The SEM images are shown in Figure 4. No obvious deformations in the structural morphology were found. The separated crystals confirm the XRD results that there is no complete or partial collapse in the framework structure of the catalysts after performing the sulfurization treatment and/or platinum metal loading on their surface.

The diameters of the parent ZrO₂, 0.5% Pt/ZrO₂, and 1% Pt/ZrO₂ crystals were found to be on the order of 33 nm with sub-cubic shaped particles. According to the published literature [37,38], platinum metal is formed on the surface of the ZrO₂ catalyst, either in the form of agglomerates at some points or dispersed at other points. In contrast, the measured diameters of the parent SZrO₂ crystals, 0.5% Pt/SZrO₂, and 1% Pt/SZrO₂ crystals exhibited modest differences, which were around 27 nm. This can be attributed to their treatment with sulfate, as this usually leads to agglomeration of the particles [5]. However, all of these particles appear to have almost the same crystal structure.

3.1.3. Energy Dispersive X-ray Analysis

Figure 5 depicts the EDX spectra of unsulfated zirconium oxide and sulfated zirconium oxide samples, loaded with 0.5 and 1 wt% Pt metal. This description demonstrates the composition of the components of the materials present on the surface of the prepared catalysts. This test was designed specifically to analyze the percentage of elements on the surface of the sample only. Analysis of the quantities of elements resulted in data that showed relative similarity in the percentages of platinum loading on the surface of both the ZrO₂ and SZrO₂ catalysts, as it was found that they were all approximately determined in the range of 0.5 to 1 wt%, which indicates the success of the metal impregnation technical procedures. In fact, part of the minimal decrease or slight increase in the percentage of metal loading can be attributed to the difference in the distribution of Pt-atoms within the pores and cavities of the nanocatalysts or to the occurrence of agglomeration in the Pt-dispersion at certain sites, depending upon the selection of spots during the EDX analysis. In addition, the SZrO₂ sample underwent EDX analysis, providing confirmation that the zirconium oxide lattice includes approximately 11.84 wt% sulfur and is evidence of successful sulfurization handling. Additional spectra obtained from EDX analysis provide information on the weight percentages of the main components included within the nanocatalyst. Inside the composition of the parent ZrO₂ catalyst, weight percentages of zirconium and oxygen elements were found to be in the range of 82.2 and 17.3 wt%, respectively. These EDX spectra also reveal the presence of trace amounts of other elements, which may be attributed to impurities, and this is consistent with the XRD analysis as the XRD patterns of the samples contain small peaks of byproducts.

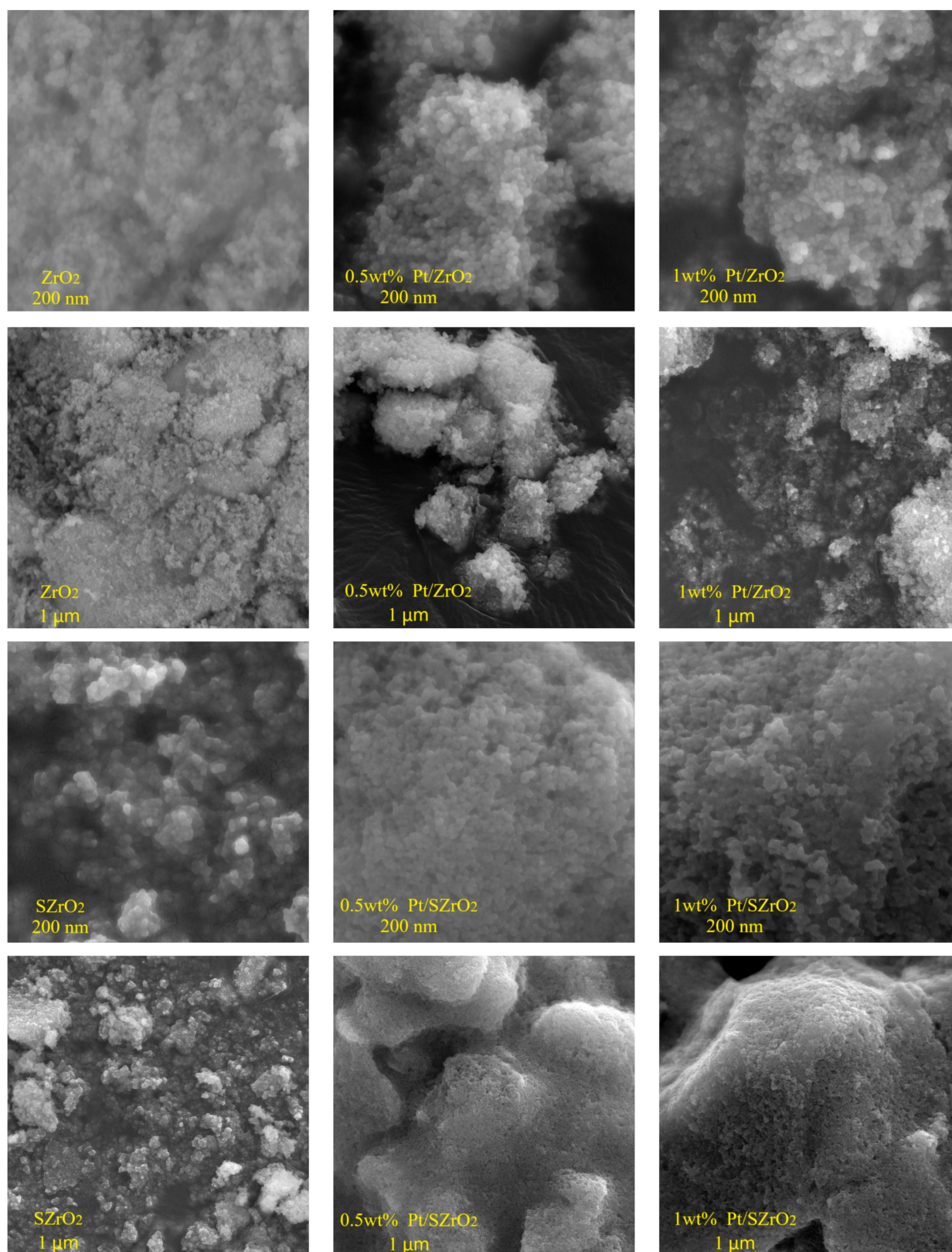


Figure 4. SEM images of nanocatalysts: ZrO₂ (top) and SZrO₂ (bottom) loaded with different percentages of Pt metals.

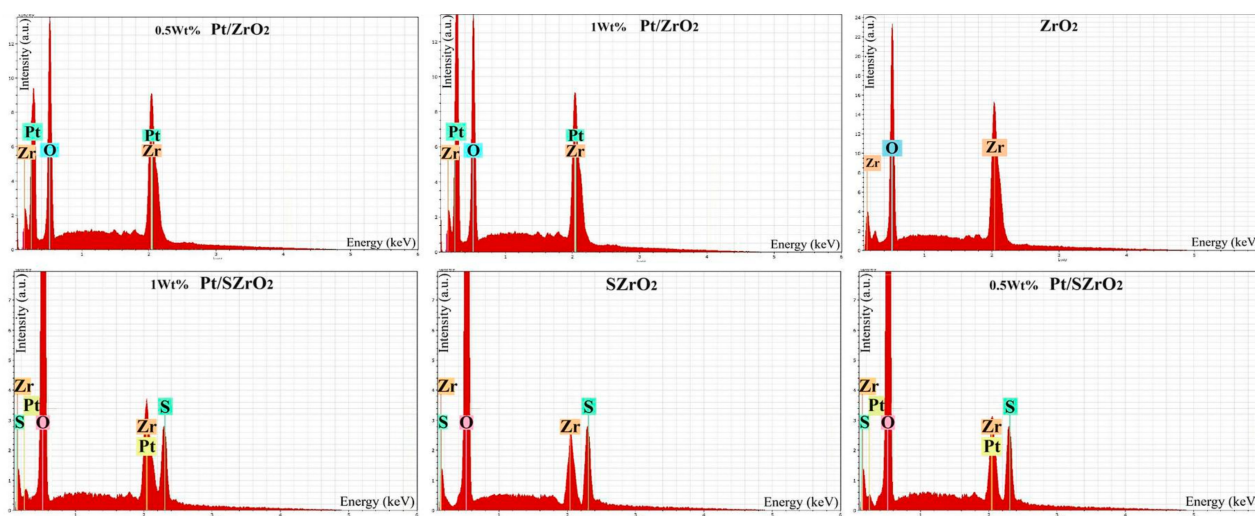


Figure 5. EDX-spectra of nanocatalysts: ZrO_2 (top) and SZrO_2 (bottom) loaded with different percentages of Pt metals.

3.1.4. BET-Surface Area Analysis

Catalyst surface area measurement was performed using the Brunauer–Emmett–Teller method, which involves physical adsorption of nitrogen gas at a temperature of 77 K. The catalyst samples underwent a preheating process at approximately 350 °C in order to remove moisture and other contaminants by out-gassing under vacuum. Next, the 8-h BET-measurement was carried out. Surface area and pore volume of the nanocatalysts are shown in Table 3.

Table 3. BET-surface area and pore volume of the as-prepared nanocatalysts.

No.	Catalysts Type	Measured Surface Area (m^2/g)	Pore Volume (cm^3/g)
1	ZrO_2	35.55	0.123
2	ZrO_2 loaded with 0.5% Pt	30.73	0.106
3	ZrO_2 loaded with 1% Pt	30.21	0.104
4	SZrO_2	24.00	0.068
5	SZrO_2 loaded with 0.5% Pt	20.98	0.059
6	SZrO_2 loaded with 1% Pt	19.72	0.056

The results of this study revealed that the parent catalysts showed a slightly larger surface area and pore volume compared to the catalysts that were treated with sulfur and loaded with metals on their surface. This observation was related to the formation of new active metal sites within the catalysts, represented by Pt, as well as the presence of active sulfuric metal sites in other catalysts, represented by Pt/S. These sites reduce the overall BET-surface area of the catalyst. In fact, increasing the metal loading on the surface of the catalyst may lead to blockage of some of the pores on its surface, and the same role can be played via the sulfate pretreatments, which limits the entry of nitrogen gas molecules into the catalyst framework structure. Consequently, this phenomenon leads to a decrease in the measured area and pore volume. The results of this study demonstrated a negative relationship between the percentages of metals loaded and/or sulfur treated and the surface area and pore size of the prepared catalysts. This observation is consistent with previous findings reported in the literature [33,39]. In more detail, the catalyst sulfate pretreatment leads to a significant decrease in both the surface area and pore volume. This is because the sulfate approach leads to a partial increase in the viscosity of the outer region (i.e., external area) of the catalyst particles, which in turn leads to a decrease in the observed available surface area, but at the same time it may play a major role in increasing catalytic activity throughout hydrogenation and dehydrogenation reactions. Furthermore, the decrease

in specific surface area is due to the calcination and high-temperature preheating of the samples during preparation, and not only due to the deposition of Pt and/or S species.

3.1.5. Fourier-Transformed Infrared Spectra Analysis

The FTIR of the parent zirconia sample and other ZrO_2 samples after loading with Pt metals [i.e., A, B, and C] were investigated within the region of $400\text{--}4000\text{ cm}^{-1}$, as shown in Figure 6. The visible absorption band in the region ranging from $2980\text{--}3435\text{ cm}^{-1}$ is attributed to the stretching vibrations of hydroxyl groups (O–H) in water molecules. On the other hand, the absorption band at 1627 cm^{-1} is indicated by the bending vibration of water molecules [40]. The composition of the detected water in these spectra remains unknown, as it is not clear whether it reflects the surface composition resulting from the heating process or whether it represents water that quickly attached to the surface during the cooling phase [41]. The peaks observed at 624 and 748 cm^{-1} may be attributed to the bending vibrations of the hydroxyl groups linked to zirconium oxide, which correspond to the Zr–O stretching vibrations [41]. In the broad band range $1230\text{--}1415\text{ cm}^{-1}$, carbonates are identified within the FTIR curves [40]. Moreover, the Pt-impregnated catalysts show characteristic peaks at wave number $1060\text{--}1248\text{ cm}^{-1}$ accompanying sulfate groups, as clearly shown in Figure 7. This is an indication that Pt metal has been impregnated into the nano-SZ and these results show consistent agreement with those published in the literature [42].

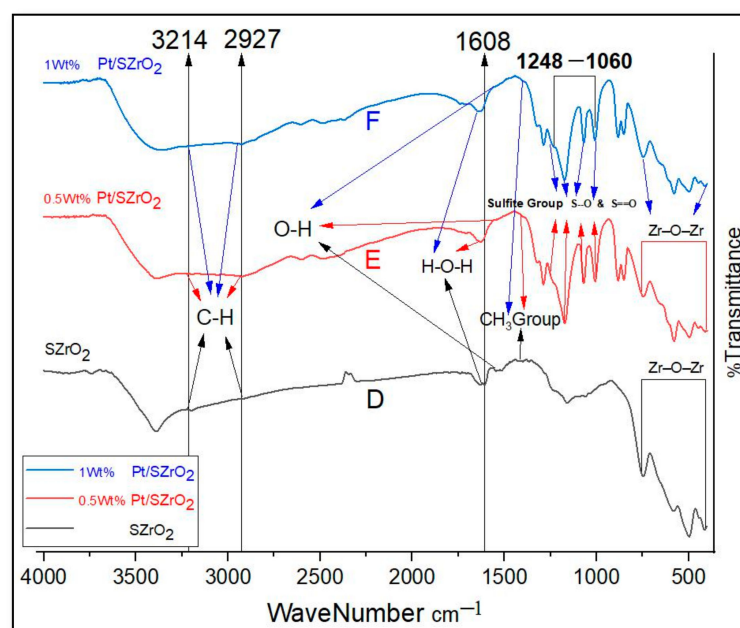


Figure 6. FT-IR spectra of the parent ZrO_2 and the prepared Pt/ ZrO_2 nanocatalysts loaded with different percentages of Pt metals.

Figure 7 depicts the Fourier transform infrared (FTIR) spectra of the parent sulfated zirconia nanoparticles and other sulfated samples after platinum metal loading [i.e., D, E, and F]. The spectral peak observed at a wavenumber of 1608 cm^{-1} is attributed to the bending vibration mode of water molecules adsorbed on the surface. Likewise, the observed peak at 1560 cm^{-1} is attributed to the O–H vibrational mode. The observed bands at around 1060 , 1074 , 1159 , and 1248 cm^{-1} are identified as symmetric and asymmetric stretching vibrations of sulfate groups, caused by symmetric S–O, asymmetric S–O, symmetric S=O, and asymmetric S=O vibrations, respectively, which are shown evidently in the FTIR-spectra of samples loaded with platinum metal. This observation indicates that the sulfate species exist in the form of bidentate complexes coordinated with ZrO_2 , wherein bidentate ligands are Lewis bases that donate two pairs (double “bi”) of electrons

to a metal atom. Similar results have also been documented in the literature [43–45]. The IR vibration peaks at 412, 447, 497, 578, 580, 582, and 746 cm^{-1} can be attributed to the characteristic vibration of cubic zirconia clusters (i.e., Zr–O–Zr). Moreover, it was shown that the vibration peak at 582 cm^{-1} is related to the distinctive vibration of tetragonal zirconia [46,47]. Moreover, the spectral peak at a wavenumber of 1398 cm^{-1} can be ascribed to the asymmetric stretching vibrations of the methyl groups (CH_3). The sample exhibited both asymmetric and symmetric stretching vibrations of methylene groups (CH_2) at wavenumbers of 2927 and 3214 cm^{-1} , respectively. These results are consistent with the results reported by Mossayeb [48]. The band positions in the spectrum of Pt/SZrO₂ show some changes compared to those seen in the spectrum of nano-SZrO₂. The presence of characteristic sulfite peaks provides convincing evidence that the ZrO₂ nanosurface has undergone modification with sulfite.

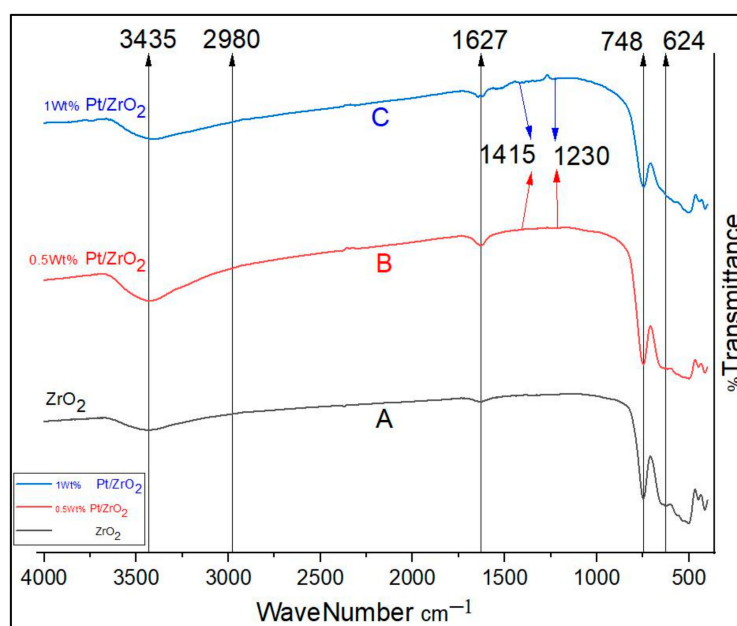


Figure 7. FT-IR spectra of the parent SZrO₂ and the prepared Pt/SZrO₂ nanocatalysts loaded with different percentages of Pt metals.

3.2. Results of Catalytic Hydroisomerization Reactions

Conversion, selectivity, and yield of *n*-heptane hydroisomerization processes were determined using experimental data obtained using six nanostructured catalysts, as previously shown in Table 2. The aforementioned equations 1, 2, and 3 were applied to derive these parameters. The results obtained experimentally are tabulated in Table 4.

Table 4. Weight ratio results for conversion, selectivity, and yield values at 230°.

Catalysts	Cat-1	Cat-2	Cat-3	Cat-4	Cat-5	Cat-6
Conversion	43.9	55.3	50.1	47.2	69.64	62.8
Selectivity	61.1	71.9	69.8	65.4	81.4	80.8
Yield	26.82	39.76	34.96	30.86	56.68	50.74

The experimental results demonstrated in Figure 8 confirm that Cat-5, which stands for 0.5% Pt/SZrO₂ catalyst, exhibited relatively high catalytic performance compared to other catalysts used in hydroisomerization reactions. It is shown that Cat-5 achieved a conversion of 69.64% and a selectivity of 81.40% toward isomers including *iso*-heptane. The findings presented in this study show a high degree of agreement with the results reported in other studies in the published literature [1]. In the context of isomers resulting from *n*-heptane hydroisomerization reactions on the surface of the Cat-5 catalyst, it was generally observed

that the dominant component among the isomers formed is *iso*-pentane ($i\text{-C}_5\text{H}_{12}$), which represents about 44.99% of the total composition of the isomers. The remaining isomers are 42.97% of *iso*-heptane ($i\text{-C}_7\text{H}_{16}$), 11.69% of *iso*-butane ($i\text{-C}_4\text{H}_{10}$), and a very small amount of *iso*-hexane ($i\text{-C}_6\text{H}_{14}$) of around 0.35% which are found within the reaction products. The sulfates on the surface of the catalyst provide high acidity and these in turn greatly enhance the conversion of hydrocarbons on its surface, compared to its sulfate-free counterpart. The acidity treatment and spatial arrangement of both acidic and metallic sites within the catalyst structural framework are expected to have a marked effect on both the quantity and quality represented by the spatial distribution of the resulting hydrocarbon product. Furthermore, this relationship is influenced by the operational conditions of the process, as documented in the literature [25]. In contrast, the overall isomer selectivity observed on the surface of non-sulfate-treated catalysts (Cat-1 to Cat-3), shows a relative decrease compared to sulfate-treated catalysts (Cat-4 to Cat-6) with equivalent properties. This is due to the marked difference in acidity as well as the surface area of the sulfate-treated catalysts over which the metal sites are distributed, as shown previously in Table 3, which may have allowed the production of relatively higher total isomer compounds than those generated on the surface of the untreated catalysts. In fact, deep sulfate treatment of catalysts causes the majority of catalysts to exhibit significant levels of acid activity, which may lead to increased undesirable reactions such as cracking and coke buildup on their surfaces. As a result, a decrease in the generation of isomers on their surface is observed during the reaction. Accordingly, the treatment of catalysts with sulfate must be very precise for the purpose of improving the catalytic properties of the catalysts [29,49].

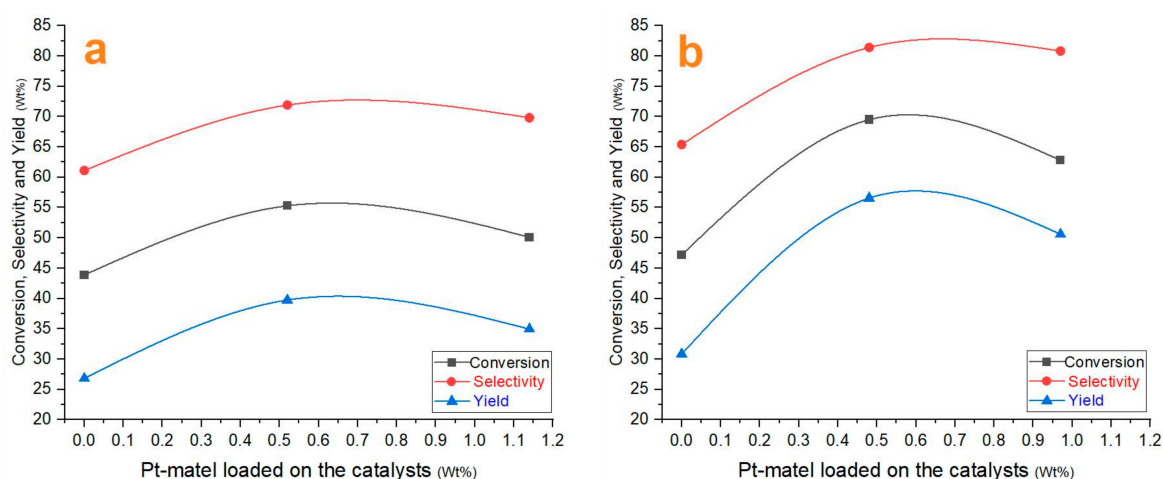


Figure 8. Catalytic performance of nanocatalysts: (a) ZrO₂ and Pt/ZrO₂ samples, and (b) SZrO₂ and Pt/SZrO₂ samples.

However, hydrogenation processes, such as the hydroisomerization reaction of *n*-heptane, often lead to a decrease in coke accumulation due to the presence of hydrogen gas, which helps to incorporate platinum (Pt) into zirconium dioxide (ZrO₂), which leads to high thermal stability, as confirmed by other researchers [40,50]. It can be noted that the catalyst not loaded with Pt-metal and not treated with sulfate (i.e., Cat-1) produces on its surface the lowest percentage of the resulting isomers. The presence of a sufficient number of metal sites on the catalyst surface is of great importance in order to maintain the hydrogenation/dehydrogenation processes, which play a crucial role in achieving high rates of resulting isomers [51]. Moreover, since sulfated zirconia (SZ) is a superacid catalyst and can activate the cracking process to produce light alkanes even at low temperatures, it suffers from rapid deactivation during the reactions as observed by the conversion and selectivity results obtained using Cat-4. The addition of some modifiers, such as several Pt-transition metals, as shown in the case of Cat-5 and Cat-6, has been proven to reduce the rapid deactivation rate compared to unmodified SZ [15]. Furthermore, by comparing

the results of both conversion and selectivity on the surfaces of sulfate-treated catalysts, i.e., Cat-5 and Cat-6, in addition to non-sulfate-treated catalysts, i.e., Cat-2 and Cat-3, it is noted that loading the catalyst with 0.5% Pt gives better results than loading it with 1% Pt. It is necessary for the platinum metal content to be at an appropriate level in order to balance the paraffin and olefin formation on the catalyst surface. Therefore, the amount of metal loaded has a major role in regulating the rate of isomerization, and this is consistent with other studies [52]. The presence of Pt-cations plays a role as Lewis acid sites and reduces the Brønsted acidity which results in lower overall acidity of the catalyst especially in the dehydrogenation mechanism and reduces coke production during the reaction [53–55]. It is not recommended to load catalysts, such as ZrO_2 and/or $SZrO_2$, with a high concentration of Pt-metal due to its ability to cause rapid hydrogenolysis of hydrocarbons, as this phenomenon leads to increased generation of low molecular weight gases which reduces the yield of isomers [56,57]. In addition, the observed low conversion on the catalyst surface when using a relatively high amount of Pt-metal can be attributed to the existence of Pt-atoms near the catalyst pores causing complete blockage of some pores as indicated in the published literature [58,59]. The distributions of the spectra of hydrocarbons resulting from the hydroisomerization reactions of *n*-heptane on the surfaces of non-sulfate-treated and sulfate-treated catalysts were investigated, as shown in Figure 9a and Figure 9b, respectively.

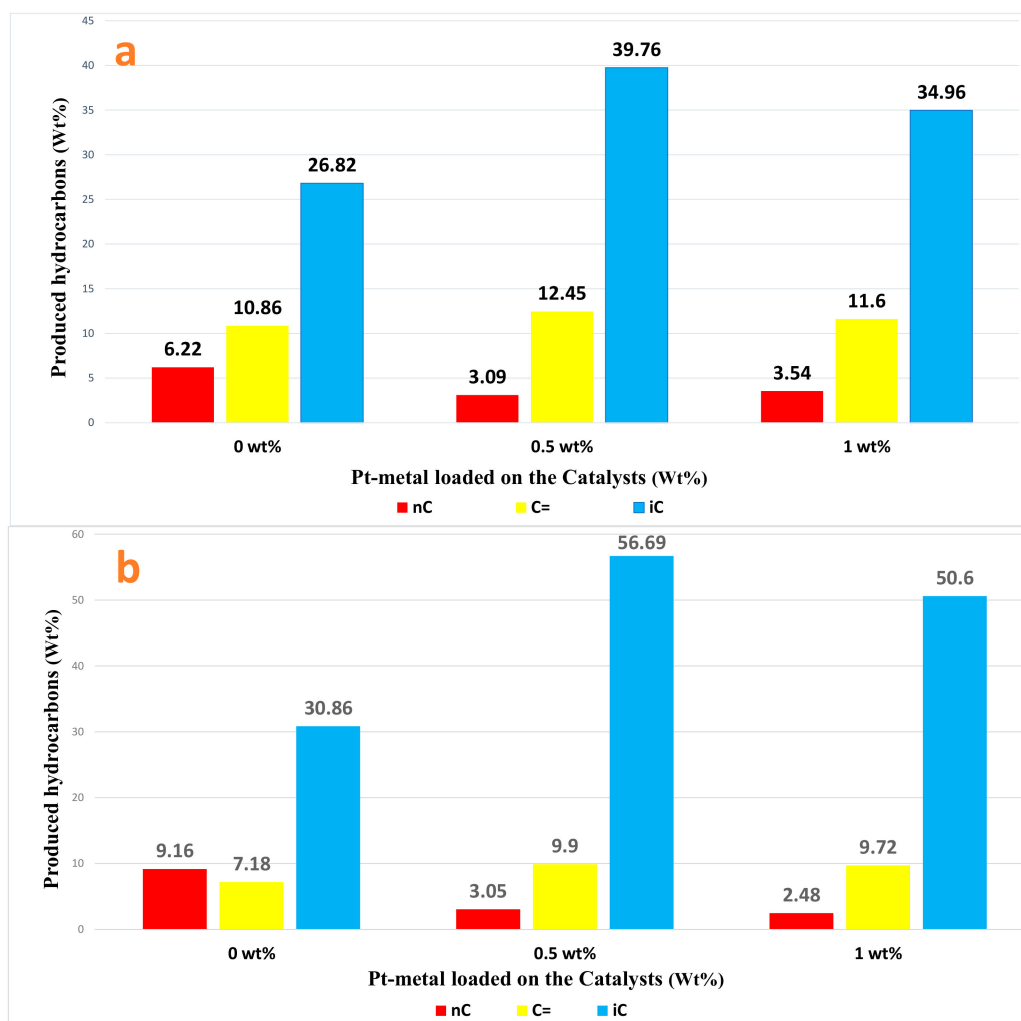


Figure 9. (a) Distribution of spectra of hydrocarbons (nC=) on ZrO_2 , 0.5% Pt/ ZrO_2 , and 1% Pt/ ZrO_2 nanocatalysts at 230 °C. (b) Distribution of spectra of hydrocarbons on $SZrO_2$, 0.5% Pt/ $SZrO_2$, and 1% Pt/ $SZrO_2$ nanocatalysts at 230 °C.

In general, it can be noted that isomers (iC: branched hydrocarbon compounds) are the most produced on the surfaces of all catalysts, followed in terms of percentage by olefins (i.e., C=: unsaturated hydrocarbon compounds contain at least one double bond), and then paraffins (i.e., nC: saturated hydrocarbon compounds contain carbon–carbon single bonds). It is known that the isomer is one of the desirable compounds, as are olefins, because olefins contain higher research octane numbers than paraffin compounds. It can clearly be observed that the lowest percentage of isomers was generated on the surface of the Cat-1 catalyst which is not treated with sulfate and is not loaded with Pt-metals. It can be noted that the highest percentage of isomers was generated on the surface of the Cat-5 catalyst which is treated with sulfate and loaded with 0.5% Pt-metals. That is, the process of acid sulfate treatment and loading the noble metal onto the surface of the ZrO₂ catalyst led to an increase in the percentage of isomers produced on its surface to more than 26%, while the conversion increased to more than 25%. This improvement in the catalytic activity of a cheap catalyst using a small percentage of metal loaded on its surface is remarkable and can be recommended as an approach in the process of developing the hydroisomerization of paraffins and contributing to raising the value of the octane number of the produced fuel.

On the other hand, the aim of this study was to obtain the highest conversion and/or selectivity, via the hydroisomerization of *n*-heptane which has the chemical formula H₃C(CH₂)₅CH₃ with an octane number of zero. Accordingly, the Cat-5 catalyst was chosen as the target catalyst, and hydroisomerization experiments were performed on its surface at three different temperatures (i.e., 200, 230, and 260 °C), as illustrated in the Table 5, in order to investigate the effect of temperature as the most essential reaction parameter on the quantity and quality of products.

Table 5. Weight ratio results for conversion, selectivity, and yield values at three different temperatures.

Temperatures	200 °C	230 °C	260 °C
Conversion	51.61	69.50	70.35
Selectivity	72.62	81.56	53.51
Yield	37.48	56.68	37.64

The data obtained regarding conversion, selectivity, and yield are shown in Figure 10. It can be noted that increasing the reaction temperature to more than 230 °C led to a very slight increase in the conversion, and at the same time the selectivity towards isomer generation decreased significantly, which naturally leads to a significant reduction in the yield. The reason for this can be attributed to an increase in the processes of hydrocarbon cracking within the structural framework of the catalyst, as increasing the temperature by about 30 °C naturally leads to an increase in the catalytic activity and an acceleration of the reaction rate. These results are consistent with what other researchers have found [1]. On the other hand, no improvement in conversion and/or selectivity was observed when the reaction temperature was reduced by 30 °C. Therefore, the temperature of 230 °C can be considered the best temperature for the *n*-hydroisomerization process using the target catalyst (i.e., 0.5% Pt/SZrO₂). The distribution of hydrocarbon spectra obtained using different temperatures is shown in Figure 11. A noticeable increase in the amount of olefins produced is observed when the reaction temperature is increased to 260 °C, with a significant decrease in the amount of isomers produced. This can be attributed to the rapid increase in the breakdown of paraffinic hydrocarbon chains (i.e., *n*-C₇) to give unstable olefin chains according to the known mechanism of cracking reactions. The *n*-heptane hydroisomerization reactions at temperatures between 230 °C and 260 °C are very complex and include four expected reaction stages, namely hydrogenation, hydroisomerization, dehydrogenation, and hydrocracking. For the purpose of investigating the reaction mechanism in depth and finding the kinetic parameters in this study, a mathematical model has been created in this regard.

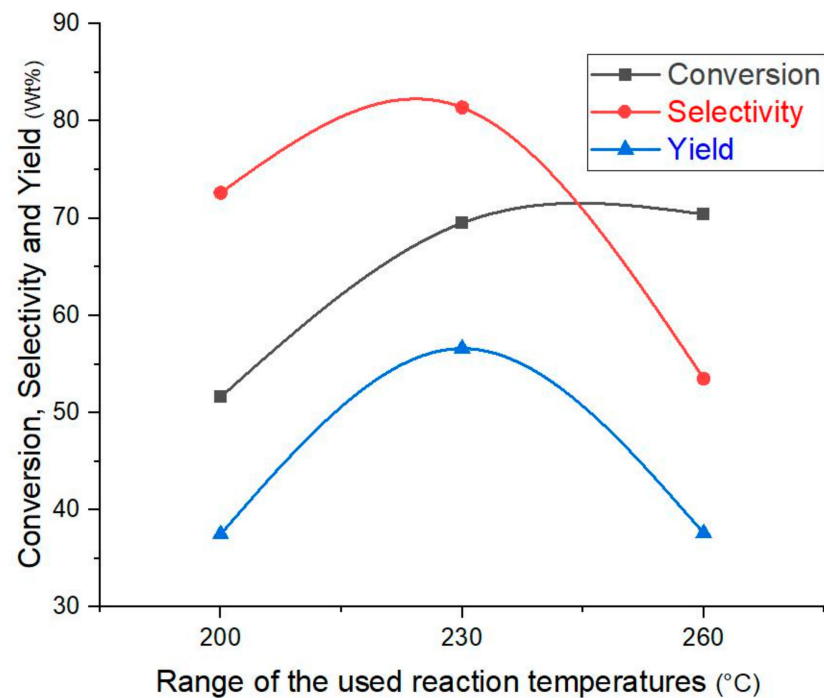


Figure 10. Conversion, selectivity, and yield at three different temperatures over 0.5 wt% Pt/SZrO₂ nanocatalysts.

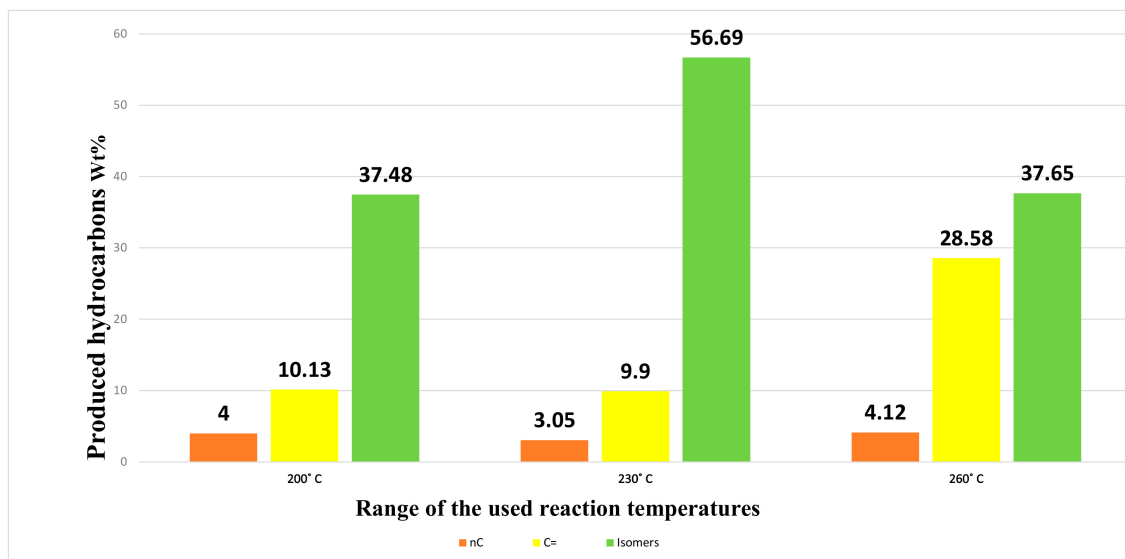


Figure 11. Distribution of spectra of hydrocarbons over 0.5 wt% Pt/SZrO₂ at three different temperatures (200, 230, and 260 °C).

4. Mathematical Modelling

4.1. Model Assumptions

The following assumptions are made to simplify the mathematical model [34,60,61]:

- Steady state isothermal plug flow reactor.
- Homogeneous gas-phase reactions.
- First order reaction rate.
- Constant pressure (Neglecting pressure drop within catalyst bed).
- Neglecting the radial distribution within the reactor.

4.2. Proposed Reaction Scheme

The proposed reaction mechanism consisting of 23 reactions and 15 components was designed as shown in Table 6 according to the predicted experimental results. Four groups of reactions are considered within the reaction scheme, namely hydrogenation, dehydrogenation, hydroisomerization, and hydrocracking, as explained in Figure 12. Hydroisomerization reactions take place at lower temperatures than those of hydrocracking reactions. Hydroisomerization reactions are exothermic and equilibrium limited. However, it should be noted that operating at low temperatures will reduce the reaction rate. For this reason, a highly active catalyst must be used, and accordingly acid sulfate treatment of the catalysts is carried out in order to improve their catalytic behavior. Although the temperature range used for the reactions in this study is relatively small (i.e., 200–260 °C) for the purpose of avoiding rapid hydrocracking reactions of hydrocarbon chains compared to the temperature range used in other studies, the appearance of light compounds such as *n*-propane and *n*-butane strongly confirms the occurrence of *n*-heptane hydrocracking reactions. Methane and ethane were not identified in the reaction mixtures because the condenser temperature was about −10 °C, which is higher than the boiling points of methane and ethane at 5 bar reactor pressure.

Table 6. The proposed reactions for mathematical modeling.

No.	Reaction	Chemical Reaction	
1	Dehydrogenation of <i>n</i> -pentane	$n\text{-C}_5\text{H}_{12} \rightarrow \text{C}_5\text{H}_{10} + \text{H}_2$	Hydrogenation/ Dehydrogenation Reactions
2	Hydrogenation of pentene	$\text{C}_5\text{H}_{10} + \text{H}_2 \rightarrow n\text{-C}_5\text{H}_{12}$	
3	Dehydrogenation of <i>n</i> -butane	$n\text{-C}_4\text{H}_{10} \rightarrow \text{C}_4\text{H}_8 + \text{H}_2$	
4	Hydrogenation of butene	$\text{C}_4\text{H}_8 + \text{H}_2 \rightarrow n\text{-C}_4\text{H}_{10}$	
5	Dehydrogenation of propane	$n\text{-C}_3\text{H}_8 \rightarrow \text{C}_3\text{H}_6 + \text{H}_2$	
6	Hydrogenation of propene	$\text{C}_3\text{H}_6 + \text{H}_2 \rightarrow \text{C}_3\text{H}_8$	
7	Skeletal hydroisomerisation of <i>n</i> -heptane	$n\text{-C}_7\text{H}_{16} \rightarrow i\text{-C}_7\text{H}_{16}$	Hydroisomerization Reactions
8	Skeletal hydroisomerisation of <i>i</i> -heptane	$i\text{-C}_7\text{H}_{16} \rightarrow n\text{-C}_7\text{H}_{16}$	
9	Skeletal hydroisomerisation of <i>n</i> -hexane	$n\text{-C}_6\text{H}_{14} \rightarrow i\text{-C}_6\text{H}_{14}$	
10	Skeletal hydroisomerisation of <i>i</i> -hexane	$i\text{-C}_6\text{H}_{14} \rightarrow n\text{-C}_6\text{H}_{14}$	
11	Skeletal hydroisomerisation of <i>n</i> -pentane	$n\text{-C}_5\text{H}_{12} \rightarrow i\text{-C}_5\text{H}_{12}$	
12	Skeletal hydroisomerisation of <i>i</i> -pentane	$i\text{-C}_5\text{H}_{12} \rightarrow n\text{-C}_5\text{H}_{12}$	
13	Skeletal hydroisomerisation of <i>n</i> -butane	$n\text{-C}_4\text{H}_{10} \rightarrow i\text{-C}_4\text{H}_{10}$	
14	Skeletal hydroisomerisation of <i>i</i> -butane	$i\text{-C}_4\text{H}_{10} \rightarrow n\text{-C}_4\text{H}_{10}$	
15	Hydrocracking of heptane	$\text{C}_7\text{H}_{16} + \text{H}_2 \rightarrow \text{CH}_4 + \text{C}_6\text{H}_{14}$	Hydrocracking Reactions
16	Hydrocracking of heptane	$\text{C}_7\text{H}_{16} + \text{H}_2 \rightarrow \text{C}_2\text{H}_6 + \text{C}_5\text{H}_{12}$	
17	Hydrocracking of heptane	$\text{C}_7\text{H}_{16} + \text{H}_2 \rightarrow \text{C}_3\text{H}_8 + \text{C}_4\text{H}_{10}$	
18	Hydrocracking of hexane	$\text{C}_6\text{H}_{14} + \text{H}_2 \rightarrow \text{CH}_4 + \text{C}_5\text{H}_{12}$	
19	Hydrocracking of hexane	$\text{C}_6\text{H}_{14} + \text{H}_2 \rightarrow \text{C}_2\text{H}_6 + \text{C}_4\text{H}_{10}$	
20	Hydrocracking of hexane	$\text{C}_6\text{H}_{14} + \text{H}_2 \rightarrow \text{C}_3\text{H}_8 + \text{C}_3\text{H}_8$	
21	Hydrocracking of pentane	$\text{C}_5\text{H}_{12} + \text{H}_2 \rightarrow \text{CH}_4 + \text{C}_4\text{H}_{10}$	
22	Hydrocracking of pentane	$\text{C}_5\text{H}_{12} + \text{H}_2 \rightarrow \text{C}_2\text{H}_6 + \text{C}_3\text{H}_8$	
23	Hydrocracking of butane	$\text{C}_4\text{H}_{10} + \text{H}_2 \rightarrow \text{CH}_4 + \text{C}_3\text{H}_8$	

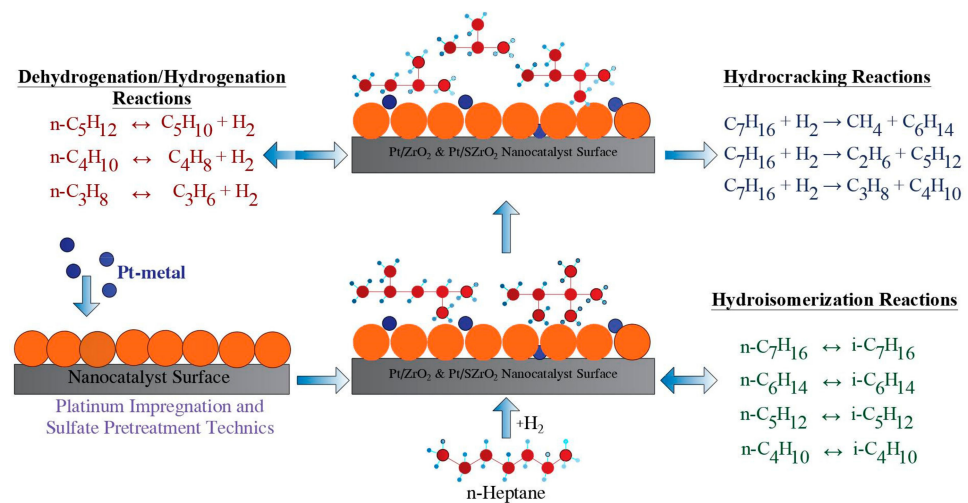


Figure 12. The proposed mechanism of hydroisomerization, hydrogenation/dehydrogenation, and hydrocracking reactions on the surface of the super-acid bi-functional nanocatalyst.

4.3. Kinetic Model

The difference in the amounts of components i with respect to the weight of the catalyst in the reactor bed was described by ordinary differential Equation (5):

$$\frac{dF_i}{dw} = \sum_j^m s_{i,j} r_j \quad (5)$$

Power law reaction kinetic was taken into account in this study and the reaction rate was estimated using Equation (6):

$$r_j = k_j P_{n,j} \quad (6)$$

The partial pressure of the i th component can be calculated according to Dalton's law of partial pressure according to Equation (7):

$$P_i = y_i \times P_t = \frac{F_i}{\sum_i^N F_i} \times P_t \quad (7)$$

The Arrhenius equation (Equation (8)) was used to represent the variation of the reaction rate constants with the temperature:

$$k_j = k_j^0 \exp\left(-\frac{E_j}{RT}\right) \quad (8)$$

In fact, Equation (5) was generalized for each component within the reaction mixture, and the reactor model involved 15 ordinary differential equations. Table 7 displays the 23 algebraic equations used to describe the rate of reactions and the 15 ordinary differential equations used to describe the rate of mass change of the 15 components within the reaction mixture.

Table 7. Algebraic and differential equations governing the rate of change in mass with the weight of the nanocatalyst.

Reaction Rate Equations	Ordinary Differential Equations
$r_1 = K_1 P_{n\text{-pentane}}$	$\frac{dF_{\text{Methane}}}{dw} = r_{15} + r_{18} + r_{21} + r_{23}$
$r_2 = K_2 P_{\text{pentene}}$	$\frac{dF_{\text{Ethane}}}{dw} = r_{16} + r_{19} + r_{22}$
$r_3 = K_3 P_{n\text{-butane}}$	$\frac{dF_{\text{Propane}}}{dw} = +r_6 + r_{17} + 2r_{20} + r_{22} + r_{23} - r_5$
$r_4 = K_4 P_{\text{butene}}$	$\frac{dF_{\text{Propene}}}{dw} = r_5 - r_6$
$r_5 = K_5 P_{\text{propane}}$	$\frac{dF_{i\text{-Butane}}}{dw} = r_{13} - r_{14}$

Table 7. Cont.

Reaction Rate Equations	Ordinary Differential Equations
$r_6 = K_6 P_{\text{propene}}$	$\frac{dF_{n\text{-Butane}}}{dw} = r_4 + r_{14} + r_{17} + r_{19} + r_{21} - r_3 - r_{13} - r_{23}$
$r_7 = K_7 P_{n\text{-heptane}}$	$\frac{dF_{\text{Butene}}}{dw} = +r_3 - r_4$
$r_8 = K_8 P_{i\text{-heptane}}$	$\frac{dF_{i\text{-Pentane}}}{dw} = r_{11} - r_{12}$
$r_9 = K_9 P_{n\text{-hexane}}$	$\frac{dF_{n\text{-Pentan}}}{dw} = r_2 + r_{12} + r_{16} + r_{18} - r_1 - r_{11} - r_{21} - r_{22}$
$r_{10} = K_{10} P_{i\text{-hexane}}$	$\frac{dF_{\text{Pentene}}}{dw} = r_1 - r_2$
$r_{11} = K_{11} P_{n\text{-pentane}}$	$\frac{dF_{i\text{-Hexane}}}{dw} = r_9 - r_{10}$
$r_{12} = K_{12} P_{i\text{-pentane}}$	$\frac{dF_{n\text{-Hexane}}}{dw} = r_{10} + r_{15} - r_9 - r_{18} - r_{19} - r_{20}$
$r_{13} = K_{13} P_{n\text{-butane}}$	$\frac{dF_{i\text{-heptane}}}{dw} = r_7 - r_8$
$r_{14} = K_{14} P_{i\text{-butane}}$	$\frac{dF_{n\text{-heptane}}}{dw} = +r_8 - r_7 - r_{15} - r_{16} - r_{17}$
$r_{15} = K_{15} P_{\text{heptane}}$	$\frac{dF_{\text{Hydrogen}}}{dw} = r_1 + r_3 + r_5 - r_2 - r_4 - r_6 - r_{15} - r_{16} - r_{17}$
$r_{16} = K_{16} P_{\text{heptane}}$	$-r_{18} - r_{19} - r_{20} - r_{21} - r_{22} - r_{23}$
$r_{17} = K_{17} P_{\text{heptane}}$	
$r_{18} = K_{18} P_{\text{hexane}}$	
$r_{19} = K_{19} P_{\text{hexane}}$	
$r_{20} = K_{20} P_{\text{hexane}}$	
$r_{21} = K_{21} P_{\text{pentane}}$	
$r_{22} = K_{22} P_{\text{pentane}}$	
$r_{23} = K_{23} P_{\text{butane}}$	

4.4. Evaluation of Kinetic Parameters

The kinetic parameters were estimated using an optimization-integration approach for the purpose of minimizing the objective function (f) shown in Equation (9), which represents the mean absolute relative error between the experimental and predicted gas compositions of the reactor effluent.

$$f = \frac{1}{n_{exp}} \sum_{i=1}^{n_{exp}} \left(\frac{1}{n_{Com}} \sum_{j=1}^{n_{Com}} \left| \frac{y_{i,j}^{exp} - y_{i,j}^{pred}}{y_{i,j}^{exp}} \right| \right) \times 100 \quad (9)$$

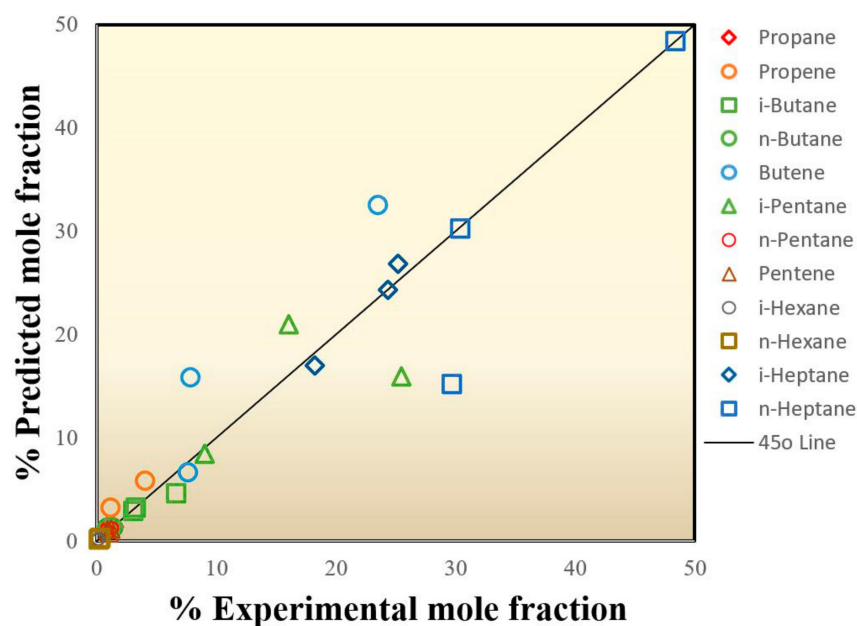
For each set of kinetic parameters, fifteen ordinary differential equations were numerically integrated using the fourth-order Runge-Kutta integration method, while a genetic algorithm optimization was used to estimate the global optimal set of kinetic parameters. Matlab *ga* and *ode45* sub-routines were used for optimization and integration, respectively.

4.5. Kinetic Modeling Results

Table 8 summarizes the comparison between the experimental results and the expected results for the three temperatures, which are 200, 230, and 260 °C. The parity plot, as illustrated in Figure 13, shows the comparison of the measured to the predicted mole fractions of the component mixture, which demonstrated a satisfactory correlation between the experimental and predicted molar fractions, with the points clustering around the diagonal line (i.e., 45-degree line) indicating an optimal fit of the model, since the deviation between the experimental values and the predicted values was minimal. Indeed, there is a good match between experimental and simulation results, especially when the global average relative error (ARE) is 13.21%. The lowest ARE value was recognized at 200 °C and was around 6.54%, which indicates that the observed model accurately simulates the molar composition of effluent products within the reaction system.

Table 8. Comparison between experimental and predicted results.

Organic Compounds/Temperatures	Experimental Results			Predicted Results			% Average Relative Error		
	200 °C	230 °C	260 °C	200 °C	230 °C	260 °C	200 °C	230 °C	260 °C
Propane	1.35	1.01	1.42	1.32	1.53	1.42	3.41	52.90	0.00
Propene	1.32	1.16	4.08	1.32	3.34	5.87	0.00	54.29	43.88
<i>i</i> -Butane	3.02	6.63	3.26	2.99	4.63	3.26	0.82	0.04	0.00
<i>n</i> -Butane	1.33	0.86	1.3	1.33	1.34	1.30	0.00	54.50	0.00
Butene	7.60	7.84	23.51	6.68	15.84	32.54	12.03	0.00	38.41
<i>i</i> -Pentane	9.05	25.51	16.04	8.45	15.99	21.00	6.63	13.60	30.90
<i>n</i> -Pentane	0.98	0.91	1.24	0.76	1.11	1.24	21.69	21.76	0.00
Pentene	1.21	0.9	0.99	1.21	1.14	0.86	0.00	26.25	12.77
<i>i</i> -Hexane	0.20	0.19	0.11	0.23	0.18	0.11	13.22	3.52	0.00
<i>n</i> -Hexane	0.34	0.27	0.16	0.39	0.27	0.15	13.97	0.00	9.48
<i>i</i> -Heptane	25.21	24.36	18.24	26.87	24.36	17.05	6.57	0.00	6.56
<i>n</i> -Heptane	48.39	30.36	29.65	48.45	30.27	15.21	0.13	0.30	48.70
% Average Relative Error							6.54	18.93	15.89

**Figure 13.** Parity plot showing the distribution of experimental versus predicted values of molar fractions for *n*-heptane conversion.

The calculated activation energies are tabulated in Table 9. The hydroisomerization reactions showed the lowest activation energy value at 23.1 kJ/mol and the highest activation energy value at 123.4 kJ/mol. The activation energies of the skeletal hydroisomerization reactions of *n*-heptane fall in the range of 25.9–50.4 kJ/mol. Moreover, the lowest activation energy value for hydrogenation reactions was found at 46.5 kJ/mol, while the highest value appeared at 212.3 kJ/mol. On the other hand, it is noted that the values of the activation energies for dehydrogenation reactions range from 43.4 to 46.7 kJ/mol. It is worth noting that the hydrogenation/dehydrogenation reactions occur successively on the metallic sites on the catalyst surface, while the hydrocracking reactions take place on the acidic sites. Through mathematical model calculations, it was found that hydrocracking reactions have

varying activation energies, reaching the highest value at 252.2 kJ/mol and the lowest value at 53.1 kJ/mol.

Table 9. Kinetic parameters of the proposed reaction scheme.

No.	Chemical Reaction	Pre-Exponential Factor (mol/bar·gm·min)	Activation Energy <i>E</i> (kJ/mol)	
1	$n\text{-C}_5\text{H}_{12} \rightarrow \text{C}_5\text{H}_{10} + \text{H}_2$	32,532.45	43.4	Hydrogenation/ Dehydrogenation Reactions
2	$\text{C}_5\text{H}_{10} + \text{H}_2 \rightarrow n\text{-C}_5\text{H}_{12}$	33,333,379	72.5	
3	$n\text{-C}_4\text{H}_{10} \rightarrow \text{C}_4\text{H}_8 + \text{H}_2$	12,892.94	46.7	
4	$\text{C}_4\text{H}_8 + \text{H}_2 \rightarrow n\text{-C}_4\text{H}_{10}$	2.72×10^{10}	212.3	
5	$\text{C}_3\text{H}_8 \rightarrow \text{C}_3\text{H}_6 + \text{H}_2$	1699.389	43.6	
6	$\text{C}_3\text{H}_6 + \text{H}_2 \rightarrow \text{C}_3\text{H}_8$	321.946	46.5	
7	$n\text{-C}_7\text{H}_{16} \rightarrow i\text{-C}_7\text{H}_{16}$	334,991.1	50.4	Hydroisomerization Reactions
8	$i\text{-C}_7\text{H}_{16} \rightarrow n\text{-C}_7\text{H}_{16}$	1195.458	25.9	
9	$n\text{-C}_6\text{H}_{14} \rightarrow i\text{-C}_6\text{H}_{14}$	186,366.5	50.4	
10	$i\text{-C}_6\text{H}_{14} \rightarrow n\text{-C}_6\text{H}_{14}$	45,113.46	42.8	
11	$n\text{-C}_5\text{H}_{12} \rightarrow i\text{-C}_5\text{H}_{12}$	94.6291	23.1	
12	$i\text{-C}_5\text{H}_{12} \rightarrow n\text{-C}_5\text{H}_{12}$	220.6853	40.7	
13	$n\text{-C}_4\text{H}_{10} \rightarrow i\text{-C}_4\text{H}_{10}$	167.6447	32.7	
14	$i\text{-C}_4\text{H}_{10} \rightarrow n\text{-C}_4\text{H}_{10}$	5.64×10^{10}	123.4	Hydrocracking Reactions
15	$\text{C}_7\text{H}_{16} + \text{H}_2 \rightarrow \text{CH}_4 + \text{C}_6\text{H}_{14}$	44,931.58	64.5	
16	$\text{C}_7\text{H}_{16} + \text{H}_2 \rightarrow \text{C}_2\text{H}_6 + \text{C}_5\text{H}_{12}$	4724.774	57.2	
17	$\text{C}_7\text{H}_{16} + \text{H}_2 \rightarrow \text{C}_3\text{H}_8 + \text{C}_4\text{H}_{10}$	5423.617	62.0	
18	$\text{C}_6\text{H}_{14} + \text{H}_2 \rightarrow \text{CH}_4 + \text{C}_5\text{H}_{12}$	3,300,815	67.6	
19	$\text{C}_6\text{H}_{14} + \text{H}_2 \rightarrow \text{C}_2\text{H}_6 + \text{C}_4\text{H}_{10}$	228,999	53.1	
20	$\text{C}_6\text{H}_{14} + \text{H}_2 \rightarrow \text{C}_3\text{H}_8 + \text{C}_3\text{H}_8$	2.99×10^{14}	252.2	
21	$\text{C}_5\text{H}_{12} + \text{H}_2 \rightarrow \text{CH}_4 + \text{C}_4\text{H}_{10}$	40,971,414	87.6	
22	$\text{C}_5\text{H}_{12} + \text{H}_2 \rightarrow \text{C}_2\text{H}_6 + \text{C}_3\text{H}_8$	3.13×10^{10}	178.1	
23	$\text{C}_4\text{H}_{10} + \text{H}_2 \rightarrow \text{CH}_4 + \text{C}_3\text{H}_8$	9×10^{13}	213.6	

According to the classical exponential law of Arrhenius, the reaction rate increases when the reaction temperature increases. The values of the pre-exponential factor (i.e., an empirical relationship between the temperature and the rate coefficient) in Table 9 represent a standard for the number of collisions that occur between reacting molecules throughout the reaction, taking into account that the activation energy is like a fingerprint for each reaction and is always positive in value. It cannot be changed unless a catalyst is present during the reaction. This is because catalysts supply a new mechanism by providing acidic and/or metallic sites that work for adsorption and dissociation reactants in order to increase reaction rates by lowering the values of activation energies without affecting in any way the possibilities for this reaction to occur (i.e., original energies) within the chemical system. Therefore, the required energy to allow for the reactants to enter the transition state to react and thereby to initiate the reaction is seen to be extensively reduced by applying the more stable and active catalyst to the reaction. It is noted from the current study that the target Cat-5 catalyst (i.e., 0.5% Pt/SZrO₂) produced the highest amount of branched hydrocarbons or isomers on its surface, as shown previously in Figures 9b and 11, meaning that it reduced the values of activation energies for the *n*-hydroisomerization reaction at a temperature of 230 °C to the lowest possible value.

The apparent activation energy of the parallel reaction was also calculated using Equation (10) [28,62], and Table 10 shows the apparent activation energies of the reactions during the *n*-heptane hydroisomerization process. Activation energies obtained from the reactions track the following order: Hydroisomerisation < Hydrogenation/Dehydrogenation < Hydrocracking. The results calculated from the mathematical model agree with the results obtained from laboratory experiments. As previously shown in Figure 11, the percentage of isomers produced on the surface of the 0.5% Pt/SZrO₂ catalyst was higher than the percentages of the remaining hydrocarbons produced at three different temperatures (200, 230, and 260 °C). It should be noted that these resulting isomers were due to hydroisomerization reactions, which had the lowest apparent activation energy of about 123.39 kJ/mol, compared with the apparent activation energies of the other reactions. It is also noted that the percentages of olefins produced on the surface of the 0.5% Pt/SZrO₂ catalyst as a result of hydrogenation/dehydrogenation reactions come in the sequence after the resulting isomers. The highest apparent activation energies of about 243.19 kJ/mol appeared for hydrocracking reactions, and these reactions are limited because the hydrocracking process requires high temperatures to overcome high activation energies [63].

$$E_{app} = \frac{E_1K_1 + E_2K_2 + \dots + E_nK_n}{K_1 + K_2 + \dots + K_n} \quad (10)$$

Table 10. The values of apparent activation energies.

Reactions	E_{app} (kJ/mol)
Hydrogenation/Dehydrogenation	212.1
Hydroisomerization	123.4
Hydrocracking	243.2

5. Conclusions

This work used mono-functional ZrO₂ nanocatalysts impregnated with two varying weight percentages of platinum metal (i.e., 0.5 and 1 wt%). The goal was to create a bi-functional nanocatalyst containing acid and metal sites. In order to enhance the acidity on the catalyst surface, other catalysts were also prepared by subjecting them to sulfate treatment and then loading them with identical proportions of Pt-metals. The catalysts were subjected to several characterization techniques to verify their physical properties. The experimentally obtained results showed that the prepared catalysts have a high catalytic behavior compared to the parent ZrO₂ catalyst. This study included a comparison to evaluate the catalytic performance of untreated sulfate catalysts with their counterparts of sulfate-treated catalysts. This evaluation was performed by studying *n*-heptane hydroisomerization reactions under a temperature of 230 °C and an operating pressure of 5 bar. Experimental results provided direct evidence supporting positive effects on catalytic activity when the acidity of the bi-functional catalyst was enhanced with sulfate. This enhancement led to an increase in the conversion of hydrocarbons on the catalyst surface and an increase in the production rate of isomers. In more detail, the reaction conversion reached about 69.64 wt% when using the 0.5% Pt/SZrO₂ catalyst compared to only about 43.9 and 55.3 wt% when using the ZrO₂ and 0.5% Pt/ZrO₂ catalysts, respectively. In contrast, the sulfate-treated bifunctional nanocatalyst showed greater selectivity towards isomer production, as the selectivity reached its highest rate of about 81.4 wt% over the surface of the 0.5% Pt/SZrO₂ catalyst, while the selectivity reached only about 61.1 and 71.9 wt% over the surfaces of the ZrO₂ and 0.5% Pt/ZrO₂ catalysts, respectively. However, it has been found that the metal loading on the catalyst surface must be carefully balanced. Although metal sites lead to improved hydrogenation and dehydrogenation reactions, an excessive increase in their concentration can reduce the surface area of the catalyst by closing the opening pores and thus promoting undesired side reactions. This may lead to a decrease in the total production of isomers. The temperature of 230 °C can be

considered the best temperature for the *n*-hydroisomerization process using the target 0.5% Pt/SZrO₂ catalyst.

It was found that increasing the reaction temperature to 260 °C or decreasing it to 200 °C leads to a decrease in the values of both the yield and the selectivity towards isomer production. The results of the mathematical model showed that the hydroisomerization reaction has the lowest apparent activation energy value of about 123.39 kJ/mol on the surface of the 0.5% Pt/SZrO₂ catalyst, which is consistent with the experimental results that demonstrated the production of the largest percentage of isomers on its surface. Apparent activation energies values obtained from the kinetic model track the following order: Hydroisomerization < Hydrogenation/Dehydrogenation < Hydrocracking.

Supplementary Materials: The following supporting information can be downloaded at: <https://www.mdpi.com/article/10.3390/chemengineering7060115/s1>, Table S1: XRD-analysis data of the ZrO₂ and Pt/ZrO₂ nanocatalysts; Table S2: XRD-analysis data of the SZrO₂ and Pt/SZrO₂ nanocatalysts.

Author Contributions: Conceptualization, M.K. and B.Y.A.-Z.; methodology, M.K.; software, Z.M.S.; validation, Z.M.S., S.J.H. and A.A.-S.; formal analysis, B.Y.A.-Z. and Z.M.S.; investigation, B.Y.A.-Z.; resources, S.J.H. and Z.M.S.; data curation, B.Y.A.-Z. and A.A.-S.; writing—original draft preparation, M.K., B.Y.A.-Z., A.A.-S. and Z.M.S.; writing—review and editing, M.K., B.Y.A.-Z. and A.A.-S.; visualization, S.J.H.; supervision, B.Y.A.-Z. and Z.M.S.; project administration, A.A.-S.; funding acquisition, M.K. and S.J.H. All authors have read and agreed to the published version of the manuscript.

Funding: This research received no external funding.

Data Availability Statement: All relevant data are included in the paper.

Acknowledgments: Thanks are extended to the institutions that provided guidance and assistance for this study, including the Department of Chemical Engineering at the University of Technology and the Oil Research and Development Centre of the Iraqi Ministry of Oil.

Conflicts of Interest: We certify that they have no affiliations with or involvement in any organization or entity with any financial interest or nonfinancial interest in the subject matter or materials discussed in this manuscript.

Nomenclature

E	Activation energy (kJ/mol)
F_i	Molar flow rate of species i (mol/min)
k_i^0	Pre-exponential factor (mol/gm _{cat} ·Min·bar)
k_i	i th reaction rate (kmol min ⁻¹)
P_i^0	Partial pressure of i th component (bar)
P_t	Total pressure (bar)
R	Universal gas constant (kJ/mol·K)
r_i	Rate of reaction (mol/gm _{cat} ·min)
S_i	Selectivity toward component i
$S_{i,j}$	Stoichiometry of reaction
t	Time (min)
T	Temperature (K)
w	Weight of catalyst (gm)
y	Mole fraction
subscript	
exp	Experimental
i	Component number
j	Reaction number
$pred$	Predicted
N	Component number

References

1. Alemán-Vázquez, L.O.; Cano-Domínguez, J.L.; Torres-García, E.; Villagómez-Ibarra, J.R. Industrial application of catalytic systems for n-heptane isomerization. *Molecules* **2011**, *16*, 5916–5927. [CrossRef]
2. Yadav, G.D.; Nair, J.J. Sulfated zirconia and its modified versions as promising catalysts for industrial processes. *Microporous Mesoporous Mater.* **1999**, *33*, 1–48. [CrossRef]
3. Normair, C.J.; Goulding, P.A.; McAlpine, I. Role of anions in the surface area stabilisation of zirconia. *Catal. Today* **1994**, *20*, 313–321. [CrossRef]
4. Song, X.; Sayari, A. Sulfated zirconia-based strong solid-acid catalysts: Recent progress. *Catal. Rev.* **1996**, *38*, 329–412. [CrossRef]
5. Utami, M.; Wijaya, K.; Trisunaryanti, W. Effect of sulfuric acid treatment and calcination on commercial zirconia nanopowder. *Key Eng. Mater.* **2017**, *757*, 131–137. [CrossRef]
6. Arata, K.; Hino, M.; Yamagata, N. Acidity and catalytic activity of zirconium and titanium sulfates heat-treated at high temperature. Solid superacid catalysts. *Bull. Chem. Soc. Jpn.* **1990**, *63*, 244–246. [CrossRef]
7. Ardizzone, S.; Bianchi, C.L.; Cattagni, W.; Ragaini, V. Effects of the precursor features and treatments on the catalytic performance of SO₄/ZrO₂. *Catal. Lett.* **1997**, *49*, 193–198. [CrossRef]
8. Busto, M.; Vera, C.R.; Grau, J.M. Optimal process conditions for the isomerization—Cracking of long-chain n-paraffins to high octane isomerizate gasoline over Pt/SO₄₂-ZrO₂ catalysts. *Fuel Process. Technol.* **2011**, *92*, 1675–1684. [CrossRef]
9. Said, A.E.-A.A.; Abd El-Wahab, M.M.; Abd El-Aal, M. The catalytic performance of sulfated zirconia in the dehydration of methanol to dimethyl ether. *J. Mol. Catal. A Chem.* **2014**, *394*, 40–47. [CrossRef]
10. Alemán-Vázquez, L.O.; Mariel-Reyes, P.R.; Cano-Domínguez, J.L. The effect of sulfates concentration in sulfated zirconia (SZ) catalysts n-heptane isomerization. *Pet. Sci. Technol.* **2010**, *28*, 374–381. [CrossRef]
11. Zalewski, D.J.; Alerasool, S.; Doolin, P.K. Characterization of catalytically active sulfated zirconia. *Catal. Today* **1999**, *53*, 419–432. [CrossRef]
12. Iglesia, E.; Soled, S.L.; Kramer, G.M. Isomerization of alkanes on sulfated zirconia: Promotion by Pt and by adamantyl hydride transfer species. *J. Catal.* **1993**, *144*, 238–253. [CrossRef]
13. Grau, J.M.; Parera, J. Single and composite bifunctional catalysts of H-MOR or SO₄₂-ZrO₂ for n-octane hydroisomerization-cracking. Influence of the porosity of the acid component. *Appl. Catal. A Gen.* **1997**, *162*, 17–27. [CrossRef]
14. Sayari, A.; Dicko, A. The state of platinum in Pt on sulfated zirconia superacid catalysts. *J. Catal.* **1994**, *145*, 561–564. [CrossRef]
15. Vijay, S.; Wolf, E.E. A highly active and stable platinum-modified sulfated zirconia catalyst: 1. Preparation and activity for n-pentane isomerization. *Appl. Catal. A Gen.* **2004**, *264*, 117–124. [CrossRef]
16. Comelli, R.A.; Finelli, Z.R.; Vaudagna, S.R.; Figoli, N.S. Hydroisomerization of n-hexane on Pt/SO₄₂^{TMTM} ZrO₂: Effect of total and hydrogen partial pressure. *Catal. Lett.* **1997**, *45*, 227–231. [CrossRef]
17. Song, Y.; Tian, J.; Ye, Y.; Jin, Y.; Zhou, X.; Wang, J.-A.; Xu, L. Effects of calcination temperature and water-washing treatment on n-hexane hydroisomerization behavior of Pt-promoted sulfated zirconia based catalysts. *Catal. Today* **2013**, *212*, 108–114. [CrossRef]
18. Pfeifer, S.; Demirci, P.; Duran, R.; Stolpmann, H.; Renfflen, A.; Nemrava, S.; Niewa, R.; Clauß, B.; Buchmeiser, M.R. Synthesis of zirconia toughened alumina (ZTA) fibers for high performance materials. *J. Eur. Ceram. Soc.* **2016**, *36*, 725–731. [CrossRef]
19. Suseno, A.; Wijaya, K.; Trisunaryanti, W.; Shidiq, M. Synthesis and Characterization of ZrO₂-Pillared Bentonites. *Asian J. Chem.* **2015**, *27*, 2619–2623. [CrossRef]
20. Ejtemaei, M.; Tavakoli, A.; Charchi, N.; Bayati, B.; Babaluo, A.A.; Bayat, Y. Synthesis of sulfated zirconia nanopowders via polyacrylamide gel method. *Adv. Powder Technol.* **2014**, *25*, 840–846. [CrossRef]
21. Tominaka, S.; Akiyama, N.; Croce, F.; Momma, T.; Scrosati, B.; Osaka, T. Sulfated zirconia nanoparticles as a proton conductor for fuel cell electrodes. *J. Power Sources* **2008**, *185*, 656–663. [CrossRef]
22. Abu, I.I.; Das, D.D.; Mishra, H.K.; Dalai, A.K. Studies on platinum-promoted sulfated zirconia alumina: Effects of pretreatment environment and carrier gas on n-butane isomerization and benzene alkylation activities. *J. Colloid Interface Sci.* **2003**, *267*, 382–390. [CrossRef] [PubMed]
23. Khalaf, Y.H.; Sherhan, B.Y.; Shakor, Z.M.; Al-Sheikh, F. Bimetallic Catalysts for Isomerization of Alkanes (A Review). *Pet. Chem.* **2023**, *63*, 829–843. [CrossRef]
24. Jiang, H.; Ni, X.; Jiang, A.; Yang, G.; Wang, L. Increase of Zr-β zeolites Lewis acidity and insights into the reactivity enhancement. *Catal. Commun.* **2023**, *183*, 106777. [CrossRef]
25. Oloye, F.F.; Aliyev, R.; Anderson, J.A. Hydroisomerisation of n-heptane over Pt/sulfated zirconia catalyst at atmospheric pressure. *Fuel* **2018**, *222*, 569–573. [CrossRef]
26. AlKhafaji, K.S.; Shakor, Z.M.; Al-Zaidi, B.Y.; Hussein, S.J. Preparation and Characterization of Metakaolin-Based Catalysts for Gasoil Hydrodesulfurization Purposes. *Arab. J. Sci. Eng.* **2022**, *47*, 6283–6296. [CrossRef]
27. Hwang, K.-R.; Ihm, S.-K.; Park, S.-C.; Park, J.-S. Pt/ZrO₂ catalyst for a single-stage water-gas shift reaction: Ti addition effect. *Int. J. Hydrogen Energy* **2013**, *38*, 6044–6051. [CrossRef]
28. Al-Iessa, M.S.; Al-Zaidi, B.Y.; Al-mukhtar, R.S.; Shakor, Z.M.; Hamawand, I. Optimization of Polypropylene Waste Recycling Products as Alternative Fuels through Non-Catalytic Thermal and Catalytic Hydrocracking Using Fresh and Spent Pt/Al₂O₃ and NiMo/Al₂O₃ Catalysts. *Energies* **2023**, *16*, 4871. [CrossRef]

29. Khalaf, Y.H.; Sherhan, B.Y.; Zaidoon, M. Hydroisomerization of n-Heptane in a Fixed-Bed Reactor Using a Synthesized Bimetallic Type-HY Zeolite Catalyst. *Eng. Technol. J.* **2022**, *40*, 1158–1170. [[CrossRef](#)]
30. Al-Iessa, M.S.; Al-mukhtar, R.S.; Sherhan, B.Y. Experimental study for converting the HDPE wastes into valuable fuel. *AIP Conf. Proc.* **2023**, *2820*, 030016.
31. Vijay, S.; Wolf, E.E.; Miller, J.T.; Kropf, A.J. A highly active and stable platinum-modified sulfated zirconia catalyst: Part 2. EXAFS studies of the effect of pretreatment on the state of platinum. *Appl. Catal. A Gen.* **2004**, *264*, 125–130. [[CrossRef](#)]
32. Ait Rass, H.; Essayem, N.; Besson, M. Selective aerobic oxidation of 5-HMF into 2,5-furandicarboxylic acid with Pt catalysts supported on TiO₂-and ZrO₂-based supports. *ChemSusChem* **2015**, *8*, 1206–1217. [[CrossRef](#)]
33. Tang, Z.; Liu, P.; Cao, H.; Bals, S.; Heeres, H.J.; Pescarmona, P.P. Pt/ZrO₂ prepared by atomic trapping: An efficient catalyst for the conversion of glycerol to lactic acid with concomitant transfer hydrogenation of cyclohexene. *ACS Catal.* **2019**, *9*, 9953–9963. [[CrossRef](#)] [[PubMed](#)]
34. Khalaf, Y.H.; Sherhan Al-Zaidi, B.Y.; Shakour, Z.M. Experimental and Kinetic Study of the Effect of using Zr-and Pt-loaded Metals on Y-zeolite-based Catalyst to Improve the Products of n-heptane Hydroisomerization Reactions. *Orbital* **2022**, *14*, 153–167. [[CrossRef](#)]
35. Saeed, A.Q.; Al-Zaidi, B.Y.; Hamadi, A.S.; Majdi, H.S.; AbdulRazak, A.A. Upgrade of heavy crude oil via aquathermolysis over several types of catalysts. *Mater. Express* **2022**, *12*, 278–287. [[CrossRef](#)]
36. Al-Zaidi, B.Y.S. The Effect of Modification Techniques on the Performance of Zeolite-y Catalysts in Hydrocarbon Cracking Reactions. Ph.D. Thesis, University of Manchester, Manchester, UK, 31 December 2011.
37. Sohail Ahmad, M.; Sadiq, M.; Aman, R. Potent heterogeneous catalyst for low temperature selective oxidation of cyclohexanol by molecular oxygen. *J. Chem.* **2016**, *2016*, 1254796.
38. Saeed, K.; Sadiq, M.; Khan, I.; Ullah, S.; Ali, N.; Khan, A. Synthesis, characterization, and photocatalytic application of Pd/ZrO₂ and Pt/ZrO₂. *Appl. Water Sci.* **2018**, *8*, 60. [[CrossRef](#)]
39. Aboul-Gheit, A.K.; El-Desouki, D.S.; Abdel-Hamid, S.M.; Ghoneim, S.A.; Ibrahim, A.H.; Gad, F.K. Sulfated zirconia catalysts for low temperature isomerization of n-pentane. *Egypt. J. Chem* **2012**, *55*, 509–527.
40. Singhanian, A.; Gupta, S.M. Nanocrystalline ZrO₂ and Pt-doped ZrO₂ catalysts for low-temperature CO oxidation. *Beilstein J. Nanotechnol.* **2017**, *8*, 264–271. [[CrossRef](#)]
41. Yakout, S.M.; Hassan, H.S. Adsorption characteristics of sol gel-derived zirconia for cesium ions from aqueous solutions. *Molecules* **2014**, *19*, 9160–9172. [[CrossRef](#)]
42. Sekewael, S.J.; Pratika, R.A.; Hauli, L.; Amin, A.K.; Utami, M.; Wijaya, K. Recent progress on sulfated nanozirconia as a solid acid catalyst in the hydrocracking reaction. *Catalysts* **2022**, *12*, 191. [[CrossRef](#)]
43. Zhai, Y.; Zhang, H.; Hu, J.; Yi, B. Preparation and characterization of sulfated zirconia (SO₄²⁻/ZrO₂)/Nafion composite membranes for PEMFC operation at high temperature/low humidity. *J. Memb. Sci.* **2006**, *280*, 148–155. [[CrossRef](#)]
44. Reddy, B.M.; Patil, M.K. Organic syntheses and transformations catalyzed by sulfated zirconia. *Chem. Rev.* **2009**, *109*, 2185–2208. [[CrossRef](#)] [[PubMed](#)]
45. Hsu, Y.-S.; Wang, Y.-L.; Ko, A.-N. Effect of sulfation of zirconia on catalytic performance in the dehydration of aliphatic alcohols. *J. Chin. Chem. Soc.* **2009**, *56*, 314–322. [[CrossRef](#)]
46. Utami, M.; Trisunaryanti, W.; Shida, K.; Tsushida, M.; Kawakita, H.; Ohto, K.; Wijaya, K.; Tominaga, M. Hydrothermal preparation of a platinum-loaded sulphated nanozirconia catalyst for the effective conversion of waste low density polyethylene into gasoline-range hydrocarbons. *RSC Adv.* **2019**, *9*, 41392–41401. [[CrossRef](#)] [[PubMed](#)]
47. Sang, X.; Zhang, L.; Wang, H.; He, D.; Deng, L.; Huang, S.; Wang, J.; Luo, Y. Influence of synthetic parameters on structural and catalytic properties of sulfated zirconia nanoparticles prepared by employing sulfate-containing anion surfactants via one-step route. *Powder Technol.* **2014**, *253*, 590–595. [[CrossRef](#)]
48. Mossayebi, Z.; Saririchi, T.; Rowshanzamir, S.; Parnian, M.J. Investigation and optimization of physicochemical properties of sulfated zirconia/sulfonated poly (ether ether ketone) nanocomposite membranes for medium temperature proton exchange membrane fuel cells. *Int. J. Hydrogen Energy* **2016**, *41*, 12293–12306. [[CrossRef](#)]
49. Al-Shathr, A.; Al-Zaidi, B.Y.; Shehab, A.K.; Shakoob, Z.M.; Aal-Kaeb, S.; Gomez, L.Q.; Majdi, H.S.; Al-Shafei, E.N.; AbdulRazak, A.A.; McGregor, J. Experimental and kinetic studies of the advantages of coke accumulation over Beta and Mordenite catalysts according to the pore mouth catalysis hypothesis. *Catal. Commun.* **2023**, *181*, 106718. [[CrossRef](#)]
50. Jiang, F.; Zeng, L.; Li, S.; Liu, G.; Wang, S.; Gong, J. Propane dehydrogenation over Pt/TiO₂-Al₂O₃ catalysts. *ACS Catal.* **2015**, *5*, 438–447. [[CrossRef](#)]
51. Benesi, H.A.; Curtis, R.M.; Studer, H.P. Preparation of highly dispersed catalytic metals: Platinum supported on silica gel. *J. Catal.* **1968**, *10*, 328–335. [[CrossRef](#)]
52. Sinfelt, J.H.; Hurwitz, H.; Rohrer, J.C. Kinetics of n-pentane isomerization over Pt-Al₂O₃ catalyst. *J. Phys. Chem.* **1960**, *64*, 892–894. [[CrossRef](#)]
53. Khurshid, M.; Al-Khattaf, S.S. n-Heptane isomerization over Pt/WO₃-ZrO₂: A kinetic study. *Appl. Catal. A Gen.* **2009**, *368*, 56–64. [[CrossRef](#)]
54. Tan, Y.; Hu, W.; Du, Y.; Li, J. Species and impacts of metal sites over bifunctional catalyst on long chain n-alkane hydroisomerization: A review. *Appl. Catal. A Gen.* **2021**, *611*, 117916. [[CrossRef](#)]
55. Kooh, A.B.; Han, W.-J.; Hicks, R.F. Kinetics of heptane reforming on Pt/L zeolite. *Catal. Lett.* **1993**, *18*, 209–218. [[CrossRef](#)]

56. Potter, M.E.; Le Brocq, J.J.M.; Oakley, A.E.; McShane, E.B.; Vandegheuchte, B.D.; Raja, R. Butane isomerization as a diagnostic tool in the rational design of solid acid catalysts. *Catalysts* **2020**, *10*, 1099. [[CrossRef](#)]
57. Ribeiro, F.; Marcilly, C.; Guisnet, M. Hydroisomerization of n-hexane on platinum zeolites. I. Kinetic study of the reaction on platinum/Y-zeolite catalysts: Influence of the platinum content. *J. Catal.* **1982**, *78*, 267–274. [[CrossRef](#)]
58. Saito, M.; Iwasaki, T. Isomerization of Pentanes on Platinum/Rare Earths-Hydrogen-Zeolite Y Catalysts. *Bull. Japan Pet. Inst.* **1976**, *18*, 117–126. [[CrossRef](#)]
59. Ribeiro, F.R. Use of platinum HY zeolite and platinum H mordenite in the hydroisomerization of n-hexane. In *Zeolites: Science Technology*; Springer: Berlin/Heidelberg, Germany, 1984; pp. 545–569.
60. Aammer, H.; Shakor, Z.M.; Al-Sheikh, F.; Al-Naimi, S.A.; Anderson, W.A. Simulation and optimization of the ethane cracking furnace using ASPEN PLUS and MATLAB: A case study from petrochemical complexes. *Combust. Sci. Technol.* **2023**, *195*, 2634–2654. [[CrossRef](#)]
61. Shakor, Z.M.; Ramos, M.J.; AbdulRazak, A.A. A detailed reaction kinetic model of light naphtha isomerization on Pt/zeolite catalyst. *J. King Saud Univ. Sci.* **2022**, *34*, 303–308. [[CrossRef](#)]
62. Soustelle, M. *An Introduction to Chemical Kinetics*; John Wiley & Sons: Hoboken, NJ, USA, 2011.
63. Al-Zaidi, B.Y.; Al-Shathr, A.; Shehab, A.K.; Shakor, Z.M.; Majdi, H.S.; AbdulRazak, A.A.; McGregor, J. Hydroisomerisation and Hydrocracking of n-Heptane: Modelling and Optimisation Using a Hybrid Artificial Neural Network-Genetic Algorithm (ANN-GA). *Catalysts* **2023**, *13*, 1125. [[CrossRef](#)]

Disclaimer/Publisher’s Note: The statements, opinions and data contained in all publications are solely those of the individual author(s) and contributor(s) and not of MDPI and/or the editor(s). MDPI and/or the editor(s) disclaim responsibility for any injury to people or property resulting from any ideas, methods, instructions or products referred to in the content.